Available online at www.sciencedirect.com
ScienceDirect
Deep-Sea Research II 55 (2008) 1139–1160
DEEP-SEA RESEARCH PART II
www.elsevier.com/locate/dsr2

Nutrient flux into an intense deep chlorophyll layer in a mode-water eddy

James R. Ledwell*, Dennis J. McGillicuddy Jr., Laurence A. Anderson

Woods Hole Oceanographic Institution, Woods Hole, MA 02543-1541, USA

Available online 7 May 2008

Abstract

An intense deep chlorophyll layer in the Sargasso Sea was reported near the center of an anticyclonic mode-water eddy by McGillicuddy et al. [2007. Eddy–wind interactions stimulate extraordinary mid-ocean plankton blooms, Science, accepted]. The high chlorophyll was associated with anomalously high concentrations of diatoms and with a maximum in the vertical profile of ^{14}C primary productivity. Here we report tracer measurements of the vertical advection and turbulent diffusion of deep-water nutrients into this chlorophyll layer. Tracer released in the chlorophyll layer revealed upward motion relative to isopycnal surfaces of about 0.4 m/d, due to solar heating and mixing. The density surfaces themselves shoaled by about 0.1 m/d. The upward flux of dissolved inorganic nitrogen, averaged over 36 days, was approximately 0.6 mmol/m^2/d due to both upwelling and mixing. This flux is about 40% of the basin wide, annually averaged, nitrogen flux required to drive the annual new production in the Sargasso Sea, estimated from the oxygen cycle in the euphotic zone, the oxygen demand below the euphotic zone, and from the ^3He excess in the mixed layer. The observed upwelling of the fluid was consistent with theoretical models [Dewar, W.K., Flierl, G.R., 1987. Some effects of wind on rings. Journal of Physical Oceanography 17, 1653–1667; Martin, A.P., Richards, K.J., 2001. Mechanisms for vertical nutrient transport within a North Atlantic mesoscale eddy. Deep-Sea Research II 48, 757–773] in which eddy surface currents cause spatial variations in surface stress. The diapycnal diffusivity at the base of the euphotic zone was $3.5 \pm 0.5 \times 10^{-5}$ m^2/s. Diapycnal mixing was probably enhanced over more typical values by the series of storms passing over the eddy during the experiment and may have been enhanced further by the trapping of near-inertial waves generated within the eddy.

Keywords: Mesoscale eddies; Ekman pumping; Mixing processes; Tracer techniques; Biological production; Nitrogen cycle

1. Introduction

Fluxes of nutrients from depth are essential to sustain phytoplankton productivity in the euphotic zone of the oligotrophic ocean, yet the mechanisms regulating those fluxes remain enigmatic. Turbulent mixing supplies nutrients to the upper ocean (Hayward, 1987; Lewis et al., 1986), but the net fluxes fall far short of the demand implied by geochemical estimates of new production (Jenkins and Goldman, 1985; Schulenberger and Reid, 1981). It has been suggested that local isopycnal uplift by mesoscale eddies and submesoscale motions cause injection of nutrients into the euphotic zone, although the integrated impact of these intermittent events is debated (Falkowski et al., 1991; McGillicuddy et al., 1998; Oschlies, 2002; Oschlies and Garcon, 1998; Williams and Follows, 2003; Levy, 2003).

There are at least two different types of eddies that generate plankton blooms in the Sargasso Sea: cyclones and mode-water eddies (McGillicuddy et al., 1999). Between these two, mode-water eddies tend to produce a stronger biological response (McGillicuddy et al., 2007). In particular, mode-water eddies appear to foster a shift in phytoplankton species composition of the deep chlorophyll maximum from picoplankton to diatom-dominated communities, which are rare in the Sargasso Sea (McNeil et al., 1999; Sweeney et al., 2003).

A number of factors favor enhanced biological activity in mode-water eddies. First, upward doming of the

*Corresponding author. Tel.: +1 508 289 3305; fax: +1 508 457 2194.
E-mail addresses: jledwell@whoi.edu (J.R. Ledwell), dmcgillicuddy@whoi.edu (D.J. McGillicuddy Jr.), landerson@whoi.edu (L.A. Anderson).

0967-0645/$ - see front matter © 2008 Elsevier Ltd. All rights reserved.
doi:10.1016/j.dsr2.2008.02.005

seasonal thermocline delivers nutrients into the euphotic zone, as is also the case in cyclones (McGillicuddy et al., 1999). Second, anticyclones (of which mode-water eddies are a special case) trap near-inertial motions by virtue of their perturbation to the local vorticity field (e.g., Kunze, 1985). Enhanced near-inertial motions augment shear, potentially leading to locally increased vertical mixing. Lastly, interactions between the surface-wind field and eddy motions create a secondary circulation with upwelling in the center of anticyclones. Although it is commonly assumed that wind stress is spatially uniform over the scale of an eddy (Stern, 1965; Niiler, 1969), mesoscale ocean currents can have a significant influence on the stress itself (Dewar and Flierl, 1987). Martin and Richards (2001) formulated a simple model for a uniform wind blowing over an idealized anticyclonic vortex, with the wind stress dependent on the difference between the air and water velocities at the sea surface. No matter which direction the wind is from, the stress will be greater on the side of the eddy where the wind opposes the surface current and less on the other side. This asymmetry leads to a greater Ekman transport on the high stress side and therefore to a divergence of surface water, which must be balanced by upwelling. In contrast, the wind-stress asymmetry for cyclonic eddies leads to downwelling, and this difference may account for the different biological communities that develop in the two kinds of eddies (McGillicuddy et al., 2007).

We describe here a tracer release experiment to study the flux of nutrients into the euphotic zone near the core of mode-water eddy A4, the focus of the EDDIES project in the Sargasso Sea during the summer of 2005 (McGillicuddy et al., 2007). A layer of patches of intense fluorescence was found deep in the euphotic zone near the center of this eddy. High chlorophyll concentrations, the highest population densities of diatoms ever recorded in the Sargasso Sea (1.2×10^5 cells/L, McGillicuddy et al., 2007), and high primary productivity occurred in this deep zone (Bibby et al., 2008), indicating that there was a flux of nutrients into the layer. Indeed, the tracer experiment showed that fluid from nutrient-rich deeper layers was carried upward by turbulent diffusion and, especially, by vertical advection. Application of the simple model of Martin and Richards (2001) and a numerical model of the eddy, presented here, show that the vertical velocity observed was of the magnitude expected to be forced by the wind-stress asymmetry at the surface of the anticyclonic eddy.

2. Methods and eddy characteristics

2.1. Navigation

Satellite altimetry data, analyzed nearly upon acquisition (Leben et al., 2002), facilitated eddy tracking prior to and during the cruises, and greatly enhanced the field campaign. Two ship-based methods were also used to estimate the position of eddy center more precisely during operations. One was to drive the ship along transit lines close to the suspected center while running the hull-mounted ADCP. The velocity vector, averaged over 5 min and over the upper 200 m (Fig. 1) could be used to identify the eddy center location within about 5 km. The second method was to use the trajectories of various drifters deployed near eddy center. Three of these were drifters drogued with holey socks set at 80 m depth. Also used for this purpose were EM-APEX floats profiling between the surface and 200 m depth, deployed by J. Girton, and a SeaHorse profiler, consisting of a float from which a wire was suspended with a weight at 200 m, with an instrument pod riding up and down the wire (Greenan, 2008). All of these devices transmitted their locations, determined with the Global Positioning System (GPS), via the ARGOS satellite system. Their tracks made rough cycloids around eddy center, but again uncertainty in the position of the center was typically about 5 km due to deviations from cycloidal motion. The trajectories of these drifters also gave an estimate of the rotation period of about 6.3 days for the inner 20 km of the eddy. Variations in the motion of the drifters led to a spread in estimates of the rotation period from about 5.5 to 7.5 days at various times. The ADCP also gave a rotation period within this range at 15–25 km from eddy center. The rotation rate is not well determined by the ADCP within 10 km because of the small velocities and uncertainty in the location of eddy center. The angular velocity decreases smoothly to 0.1 rad/d as the radius increases to 100 km. The propagation of eddy center was approximately 5 km/d a little south of west during the experiment.

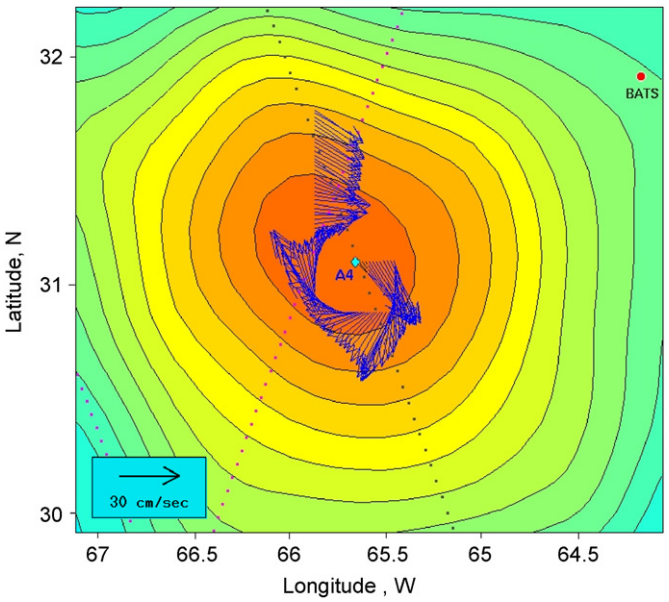

Fig. 1. Sea level anomaly (color shading) and shipboard ADCP velocities, averaged over the upper 200 m, in Eddy A4, 21 June 2005. BATS: the Bermuda Time Series Station. The sea level anomaly is estimated from all available satellite crossings using objective analysis in time as well as space.

2.2. Hydrography

Hydrographic measurements were made with a CTD/Rosette system, with 24 10-l Niskin bottles. Temperature and conductivity were measured with two pairs of SeaBird Electronics sensors on the 9*plus* CTD, the ambient water being pumped through both pairs. Also in the system were a WetLabs ECO-AFL chlorophyll fluorometer, a SeaBird SBE43 Oxygen Sensor, and a Biospherical Instruments QSR-2240 PAR sensor. Shipboard measurements of extracted pigments with a Turner fluorometer (Knap et al., 1993) showed that near eddy center about 35% of the signal from the WetLabs fluorometer was due to phaeopigments, while most of the remainder was from chlorophyll *a*; the correlation coefficient between chlorophyll *a* plus phaeopigments and fluorescence signal was 0.94. We shall report the output from the fluorometer as relative fluorescence units (RFU). Chlorophyll *a* concentrations were approximately 65% of RFU, in μg/l, according to the shipboard measurements. Subsequent analysis of HPLC pigments confirmed these trends (data available at http://ocb.whoi.edu/eddies.html).

At the core of the eddy, between 100 and 600 m depth, was a bolus of weakly stratified water with potential density anomaly, σ_θ, between 26.25 and 26.5 kg/m^3 (Figs. 2A and 3). Deep density surfaces dipped downward near the center of the eddy, and the associated pressure field dominated eddy rotation, making it anticyclonic, or clockwise. Shallow density surfaces rose toward the surface near eddy center, indicating that this clockwise flow weakened with decreasing depth.

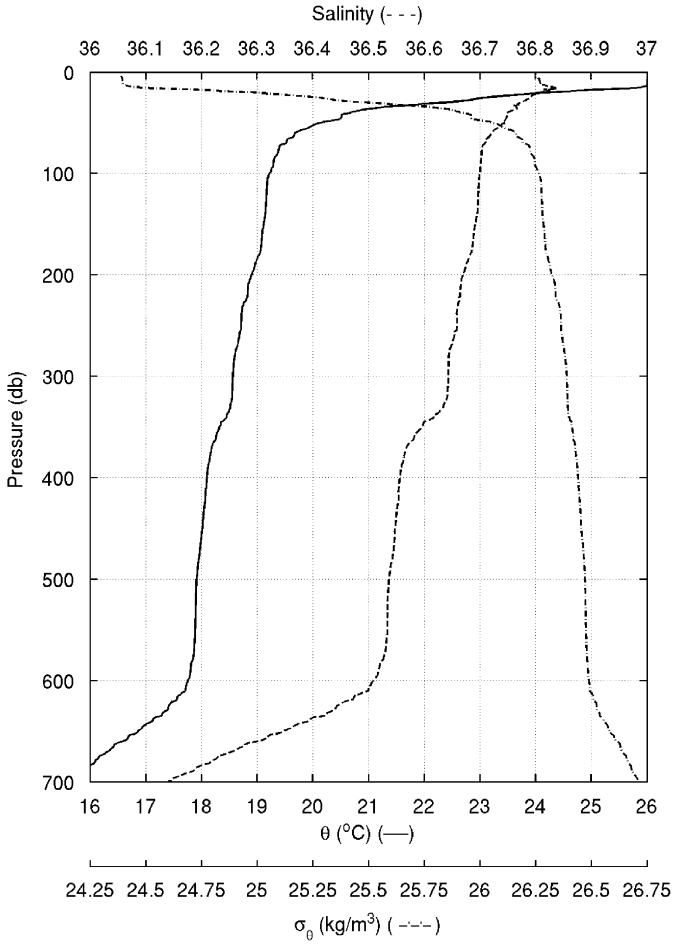

Fig. 3. Profiles of potential temperature (θ), salinity, and potential density anomaly (σ_θ) obtained at Station 31 (see Fig. 2) near eddy center, on 4 July 2005.

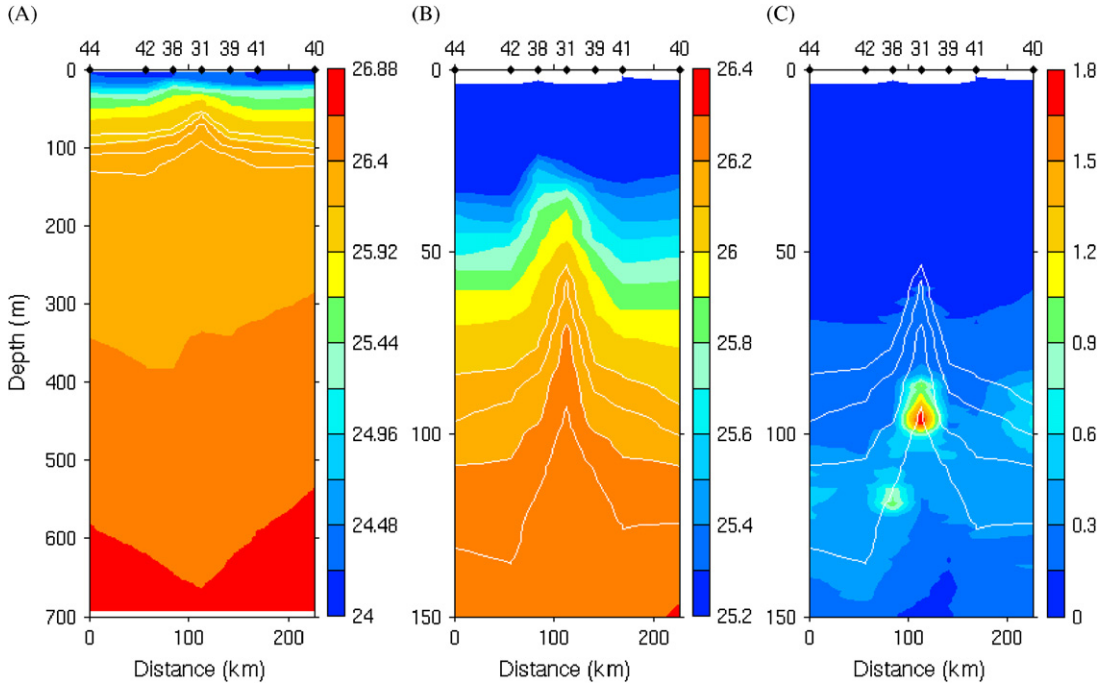

Fig. 2. Cross sections of potential density anomaly, σ_θ, and fluorescence, from stations occupied 4–6 July 2005 during cruise OC415-1. CTD station locations are indicated along the top axis. (A) σ_θ (kg/m^3); (B) σ_θ (kg/m^3) and (C) fluorescence (RFU).

Fluorescence was elevated within the eddy, and especially within the central 20 km, with the deep maximum on the $\sigma_\theta = 26.255\,kg/m^3$ surface, typically between 80 and 100 m depth at eddy center (Fig. 2C). Even higher fluorescence signals were recorded during the tracer injection and sampling tows, described later. The depth of the $\sigma_\theta = 26.255\,kg/m^3$ surface outside the eddy was approximately 130 m, below the euphotic zone. Outside the eddy the dissolved inorganic nitrogen (DIN) concentration on this isopycnal surface was typically greater than 1 μmol/kg. Near eddy center DIN was around 0.5 μmol/kg on this surface, and dropped sharply through the chlorophyll layer (Fig. 4).

Three sets of hydrographic data obtained with CTD casts during the EDDIES experiment were used for interpretation of the tracer experiment (Table 1). The first was obtained during R/V *Oceanus* Cruise OC415-2, in conjunction with the tracer injection and initial survey, centered around 31 July 2007. The second was obtained during OC415-3, which was a survey of the hydrography and plankton in Eddy A4, centered around 17 August 2007. The third set was obtained during OC415-4, in conjunction with the final tracer survey, centered around 5 September 2007.

2.3. The tracer

Sulfur hexafluoride (SF_6) was used for the tracer release experiment. The vapor pressure of pure SF_6 is about 2 MPa at 19.3 °C, the ambient temperature at the release level, while the ambient pressure was less than 1 MPa. If droplets of pure SF_6 were injected they would burst into bubbles and rise toward the surface. To avoid this, the SF_6 was mixed in a 1:9 ratio by weight with trichlorotrifluoroethane (CFC-113) to lower the vapor pressure. Even then, because of its higher solubility in water, the CFC-113 in the droplets was expected to dissolve faster than the SF_6, so that the droplets would become more concentrated in SF_6

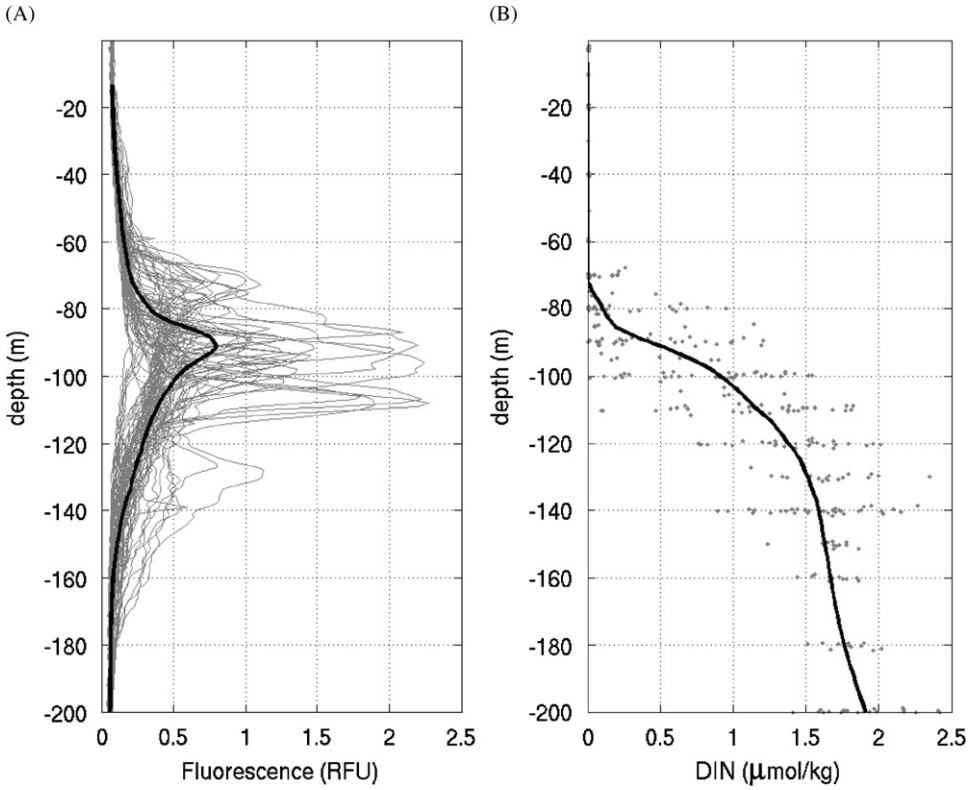

Fig. 4. (A) Individual and mean vertical profiles of fluorescence and (B) a scatter plot and mean profile of dissolved inorganic nitrogen (DIN). Observations taken from June to September 2005 were averaged at standard potential density levels and then transformed to depth using the mean depth of those isopycnal surfaces.

Table 1
Summary of cruises

Cruise	Dates in 2005	Description	Nominal survey date
OC 415-2	18 July–4 August	Tracer injection and initial survey	31 July
OC 415-3	7–26 August	Hydrographic and plankton survey	17 August
OC 415-4	29 August–15 September	Tracer final survey	5 September

as they dissolved. Consequently, the tracer mixture was injected through 25-μm diameter ceramic orifices, half the diameter used in previous injections (e.g., Ledwell et al., 1998), to insure that bubbles formed would be small enough to dissolve before rising more than a meter or so toward the surface. Watson et al. (1987) estimated the sinking distance for dense dissolving droplets; the same approach can be used to estimate approximate rise distances for dissolving bubbles.

2.4. Tracer release

The tracer was released on 23 July 2005 in two streaks along the tracks shown in Fig. 5, within 20 km of eddy center. The injection system, described in more detail by Ledwell et al. (1998), was deployed at the starboard waist of R/V *Oceanus* and towed at approximately 0.5 m/s, with the ship's course and heading chosen to keep the wire off the hull. Data from a Sea-Bird 9*plus* CTD, incorporated in the injection system, were used in a winch control system to keep the injection package close to the $\sigma_\theta = 26.255\,\mathrm{kg/m^3}$ surface, where the fluorescence maximum resided. The WetLabs fluorometer was moved from the CTD/rosette package to the injection sled prior to injection. Six 1.2-L Niskins were tripped along the injection track for salinity calibration. The release system included two injection pumps for redundancy. Four 25-μm orifices were installed on the outlet of each pump, instead of one 50-μm orifice, to achieve a flow rate of approximately 8 ml/min at the working pressure of the pumps (10–20 MPa). Despite efforts to keep the system clean, including filters installed in the lines at various points, the orifices tended to clog over time. As a result, the injection rate diminished along the first and longer of the two injection streaks shown in Fig. 5, i.e. the one that starts about 20 km north of eddy center. The flow rate during the second injection streak, near eddy center, was steady, but that streak was cut short by an approaching storm during which the ship left the eddy. A total of 1.57 kg of SF_6 was released: 0.95 kg on the first track, and 0.62 kg on the second track. The mean potential density anomaly of the water was $\sigma_\theta = 26.255\,\mathrm{kg/m^3}$, while the root mean square spread in density, due to the finite response time of the winch control system, was $0.0017\,\mathrm{kg/m^3}$. The mean vertical potential density gradient at the level of the injection was approximately $0.0024\,\mathrm{kg/m^4}$, so the root mean square control error corresponds to less than 1 m in the mean potential density gradient.

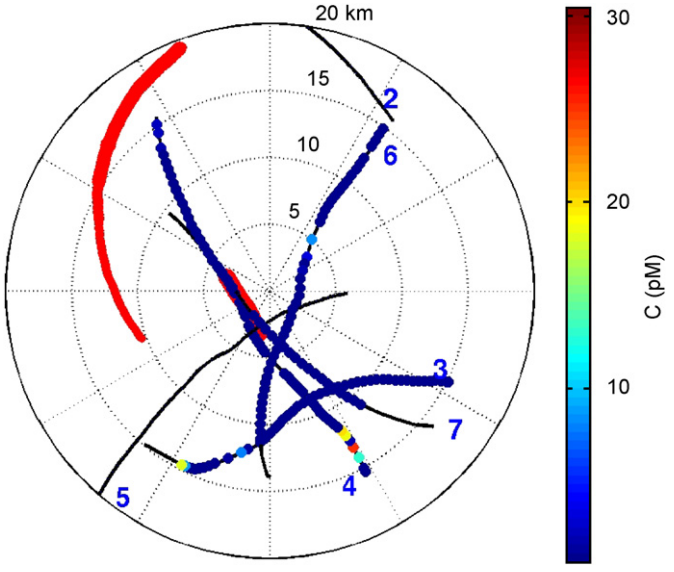

Fig. 5. Injection streaks (red) and sampling tracks for the initial survey. The small filled circles along the sampling tracks represent syringes in the 50-chamber sampler that successfully filled. The sampler failed for tracks 2 and 5, but vertical profiles were obtained. The color of the circles indicates the amount of tracer found in the syringes.

2.5. Tracer sampling

The tracer patch was sampled with a towed array of integrating samplers similar to that described by Ledwell et al. (1998). It was necessary to tow this array from the starboard waist of the ship, so the direction of the tows was constrained by the need to keep the wire off the hull. The tow speed varied from 0.6 to 0.9 m/s. At the center of the array was the CTD with WetLabs fluorometer, again for control of the winch to keep the center of the array near a target potential density surface, and again with six 1.2-L Niskin bottles on a rosette pylon for salinity calibration. Also at the center of the array was a set of 50 100-mL glass syringes, modified to be driven hydraulically (Ledwell et al., 1998). These syringes filled to 60 mL, one after the other, each one taking 12.4 min to fill. Twenty integrating samplers were hung on the wire above and below the center of the array (Ledwell et al., 1998). These samplers were adjusted to take in water slowly over 10 h as the array was towed over a track 25–30 km long, and were tripped by messenger weights. Two integrating samplers mounted on the sled at the center of the array were tripped with the aid of the rosette pylon. The same system was used for the final survey, about 40 days after the release, except that the WetLabs fluorometer was replaced by a Chelsea Instruments fluorometer, so that the former could remain on the CTD/rosette frame for most of the cruise. The two fluorometers were intercalibrated on the first sampler tow.

2.6. Tracer analysis

The samples were retrieved and analyzed with a gas chromatograph equipped with an electron capture detector. Water from the integrating samplers was transferred to 100-mL glass syringes and then analyzed by the head space method described by Wanninkhof et al. (1991), for the initial survey, when concentrations were very high, and by the purge and trap method described by Law et al. (1994) for the final survey, with a sample volume of 75 mL. Samples from the 50-syringe system at the center of the array were analyzed by the head space method for both surveys.

3. Experimental results

3.1. Initial survey

The first survey of the tracer commenced on 28 July 2005, about 5 days after the release, and continued until 2 August 2005, with one sampler tow performed each day. The six tracks occupied are shown in Fig. 5, with the concentrations found in the 50-chamber sampler shown in color. An attempt has been made to plot the tow tracks in a coordinate system that follows eddy center and rotates with the eddy with a period of 6.3 days. Of course, the rotation rate was not uniform in either time or space, and so this attempt is crude. Note, for example, that little or no tracer was found where tracks 4 and 7 overlap the inner injection streak.

Data from the 50-chamber sampler indicate that the lateral distribution of the tracer was very inhomogeneous. There was a strong streak of tracer between 11 and 14 km from eddy center along track 4. Even narrower patches were found along tracks 3 and 6. Relatively little tracer was found within 5 km of our best estimates of the location of eddy center, despite 40% of the tracer having been released there. The need for using a towed system rather than spot samples taken with a conventional rosette system is apparent from the patchiness seen here.

A single vertical profile was obtained from each sampler tow, since each of the samplers on the wire took in only one sample, albeit over a long track. The resulting profiles are shown in Fig. 6, along with their mean. The vertical coordinate on these graphs is the height above the isopycnal surface of the injection. Thus, although the central samples were taken nearly on an isopycnal surface, the others are from a spread in potential density due to temporal and spatial variations in the vertical density profile caused by internal waves, mixed patches, intrusions, or other sources of fine structure.

The peak of the mean profile was found to be approximately 2 m below the target surface (Fig. 6). This offset may result from sinking of the tracer plume due to its density anomaly before entrainment of ambient water brought it to a neutral level. Whatever the cause of the displacement of the tracer, the mean profile in Fig. 6 will be taken as the initial condition for the experiment.

3.2. Final survey

The tracer patch was sampled again between 31 August and 11 September 2005 (Fig. 7). The search concentrated on the inner 30 km of the eddy. Excursions beyond this radius found little tracer (see Tracks 5, 7, 10, and 11 in Fig. 7). The distribution of the tracer found within 30 km suggests that most of the tracer was still within that radius, but a map is not possible with the available data. Tracer was more widely distributed than in the first survey, but the patchiness is still striking. As in the first survey, relatively little of the tracer was found within 5 km of eddy center.

Vertical profiles from the integrating samplers for the 11 tows for the second survey are shown in Fig. 8, along with their mean. The tracer had spread vertically, and the peak of the tracer distribution had risen from 2 m below the $\sigma_\theta = 26.255\,\mathrm{kg/m^3}$ surface to 10 m above it in the 36 days between the initial and final surveys. Note that the times assigned to the surveys are mean times of all the tows, weighted by the amount of tracer found. Not all the tows were centered at the potential density of the release. The target σ_θ for tow 1 was $26.261\,\mathrm{kg/m^3}$, about 4 m deeper than the injection surface, because we guessed that the

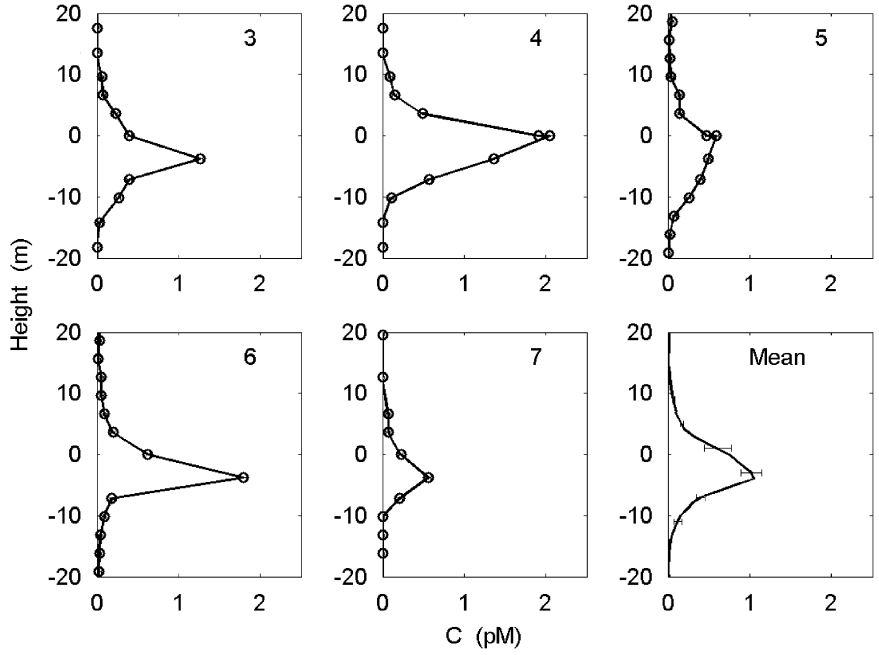

Fig. 6. Tracer profiles from each track in the initial survey and the mean profile. Height is relative to the $\sigma_\theta = 26.255\,\mathrm{kg/m^3}$ surface.

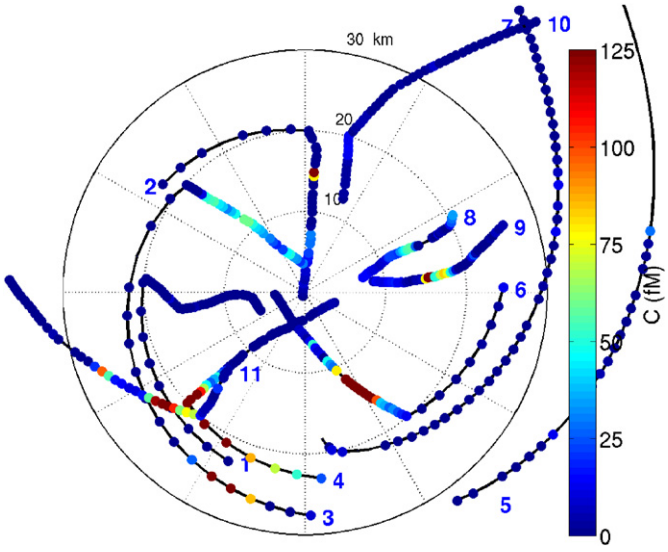

Fig. 7. Sampling tracks for the final survey, plotted in a coordinate system rotating with the core of the eddy. Tracks are labeled 1 through 11. The small filled circles along the sampling tracks represent syringes in the 50-chamber sampler that successfully filled. The color of the circles indicates the amount of tracer found in the syringes.

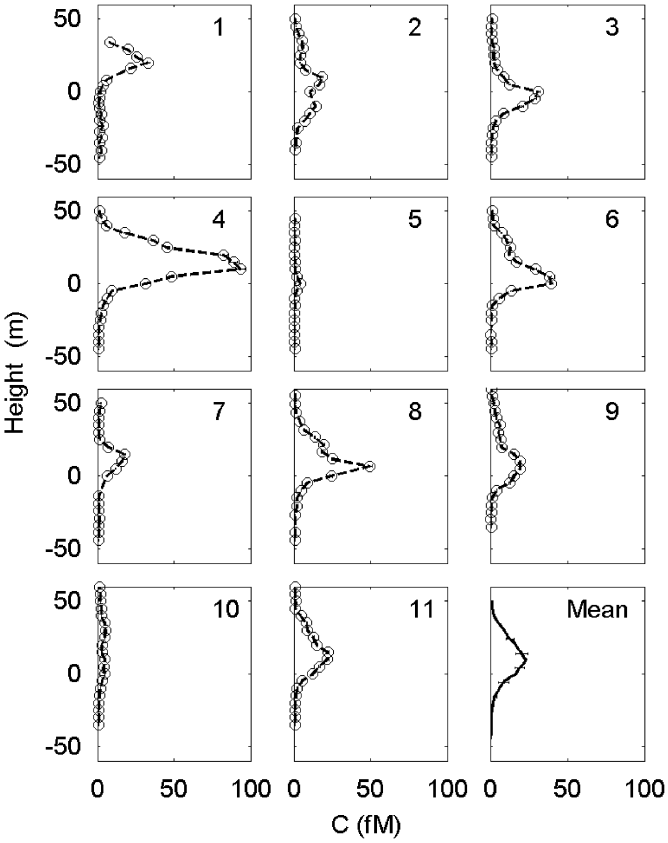

Fig. 8. Tracer profiles from each track in the final survey, and the mean profile. Height is relative to the $\sigma_\theta = 26.255\,\mathrm{kg/m^3}$ surface, whose level was estimated for Tracks 1, 9, 10, and 11 (see text).

tracer would be centered there. Tows 2 through 8 were centered at $\sigma_\theta = 26.255\,\mathrm{kg/m^3}$, the target for the injection. The target σ_θ for tows 9, 10, and 11 was $\sigma_\theta = 26.225\,\mathrm{kg/m^3}$, about 10 m shallower than the injection surface, because by the time these tows were done we were confident that the tracer had shoaled relative to the density surfaces. The reference level, $z = 0$, in the panels of Fig. 8 for these tows does not represent the level of the central sampler, but is an estimate of the average level of the $\sigma_\theta = 26.255\,\mathrm{kg/m^3}$ surface during the tow.

3.3. Radial distribution of the tracer

The distribution of the tracer injected as a function of distance r from eddy center is shown in the top panels of Fig. 9. The radial distribution estimated from the tracer for the initial and final tracer surveys are plotted in the middle and bottom panels, respectively. In the case of the injection the distribution is well known, while uncertainties are large for the surveys because of limited sampling in combination with streakiness of the tracer distribution.

Table 2 lists estimates of the moments of the tracer distribution: the total amount of tracer, the mean distance r from eddy center and the mean square distance. Again, these moments are well known for the injection. If the tracer found as a function of radius is extrapolated azimuthally for the initial survey, the estimated sum of the tracer found inferred is 2.8 kg, as opposed to the 1.6 kg known to have been released. The difference illustrates the error of the extrapolation; in this case we must have towed through relatively rich streaks of tracer. For the final survey, the extrapolation over all azimuths for the amount "found" gives 0.5 kg, only 30% of the amount injected. In this case we must have missed the richest tracer streaks. The first and second moments are of course also subject to large errors, a formal estimate of which is impossible to make.

The tracer seemed to vacate the central 10 km of the eddy between the time of injection and the initial survey, carried out between 5 and 10 days later, though sampling was admittedly limited. Coverage of the inner 10 km of the eddy in the final survey appears to have been quite good, at least with the rotation rate we have used to plot the tow tracks (Fig. 7). Nonetheless, there was still relatively little tracer found there at this time. Neither the mean radius nor the mean square radius changed significantly between the injection and the first survey, though the distribution did change. We estimate that the mean radius grew from 12 to 20 km from the injection to the final survey, however, and that the mean square radius grew from 181 to 455 $\mathrm{km^2}$. Note that the mean radius is positive definite, and is more closely related to the second moments than the first moments of the distribution in Cartesian coordinates; the first moments are identically zero under the assumption of azimuthal symmetry made in our azimuthal extrapolations.

3.4. Fluorescence along the tow tracks

The fluorometer mounted on the injection and sampling sleds gave information on the distribution of fluorescence in the central part of the eddy, over tracks as long as 30 km.

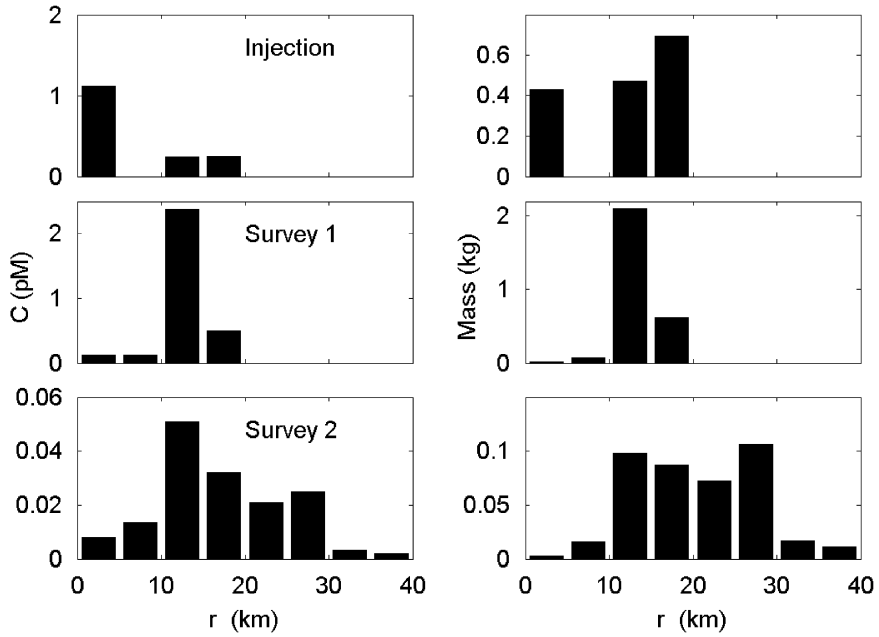

Fig. 9. Radial distribution of the tracer. The panels on the left show the average vertically integrated concentration as a function of the distance r from eddy center, known accurately for the injection and estimated from the available data for the surveys. The panels on the right give the product of the vertically integrated concentrations and the area of the annuli to which they are assigned, assuming that the radial distribution in the integrating samplers was the same as in the 50-chamber sampler.

Table 2
Radial distribution of the tracer

	Time since injection (d)	Mass injected or found (kg)	Mean r (km)	Mean r^2 (km^2)
Injection	0	1.6	12.0	181
Survey 1	8	2.8	13.4	186
Survey 2	44	0.5	20.2	455

Since our aim was to release the tracer on the isopycnal of the maximum chlorophyll concentration, the injection tows and many of the sampling tows yielded statistics along this surface. The distribution was found to be quite patchy, with peak fluorescence greater than 1 RFU in patches from 1 to 5 km across (Figs. 10 and 11), twice as high as the maximum values measured with the lowered CTD (See Section 2.2). These high fluorescence values are apparently the result of an enhanced supply of nutrients due to mixing and upwelling at the base of the euphotic zone of this mode-water eddy. The reason for the patchiness of the fluorescence is an interesting subject beyond the scope of this paper, but may be associated with submesoscale instabilities mentioned in Section 4.3 in the context of along-isopycnal mixing.

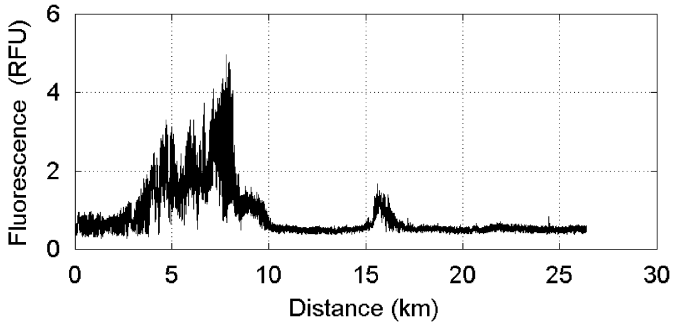

Fig. 10. Fluorescence along sampling tow 6 of the initial survey (see Fig. 11). Distance is measured from the north end of the streak. This tow yielded the highest instantaneous fluorescence.

4. Analysis

4.1. Diapycnal diffusivity and velocity

The evolution of the vertical distribution of the tracer can, with certain simplifications, be described by the equation:

$$\frac{\partial \bar{c}}{\partial t} + \left(\bar{w}_{\mathrm{d}} - \frac{\partial K}{\partial h}\right)\frac{\partial \bar{c}}{\partial h} + \frac{\partial}{\partial h}\left\{\left(\frac{\partial h}{\partial t}\right)_{\sigma}\bar{c}\right\} + \frac{\partial \bar{w}_d}{\partial h}\bar{c} = K\frac{\partial^2 \bar{c}}{\partial h^2} \quad (1)$$

where $\bar{c}(h)$ is the tracer concentration at height h above the target isopycnal surface, averaged over an area encompassing the tracer patch; t is time, $\bar{w}_{\mathrm{d}}$ is the area-averaged velocity normal to, and relative to, the mean isopycnal surfaces, i.e. the diapycnal velocity, and K is the diapycnal diffusivity of the tracer, which represents small-scale mixing processes. This equation was derived from the three-dimensional (3-D) tracer conservation equation by Ledwell et al. (1998 their Eq. (7)), except that there the last

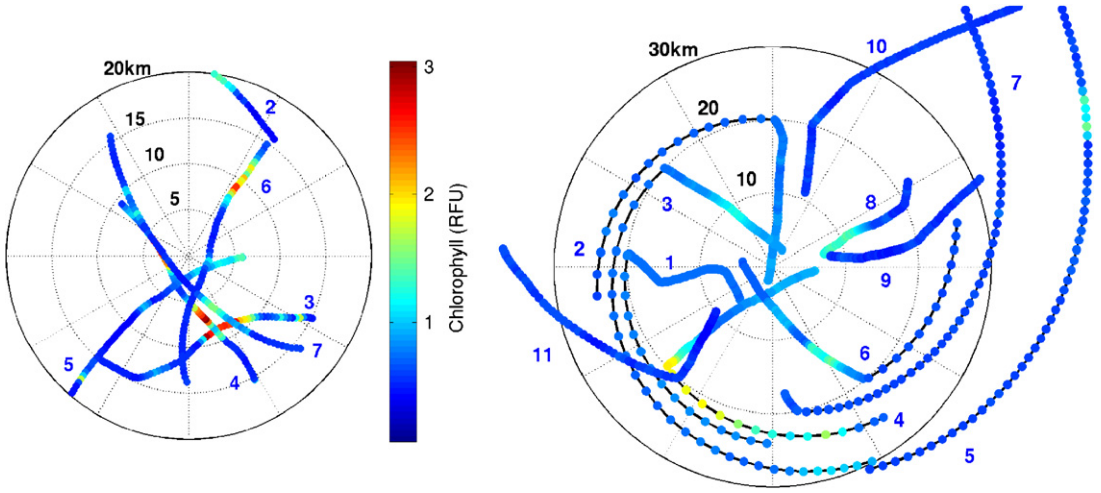

Fig. 11. Fluorescence in RFU along the tracks for the initial tracer survey (left) and the final survey (right). The color scale applies to both panels.

term on the left-hand side, involving the divergence of the diapycnal velocity, was assumed to vanish. Because the tracer concentration vanishes at the boundary of the averaging area, there are no contributions to this averaged equation from along-isopycnal advection or mixing. The distance between isopycnal surfaces is assumed to be uniform over the averaging area, once mixing events and internal waves are averaged over. Small geometric terms due to curvature of the mean isopycnal surfaces are neglected in Eq. (1).

To simplify Eq. (1) let us define the area-average velocity relative to the target isopycnal surface $\bar{w}_1$ as

$$\bar{w}_1 \equiv \bar{w}_d + \left(\frac{\partial h}{\partial t}\right)_\sigma \tag{2}$$

Then Eq. (1) can be rewritten, with some rearrangement of terms as

$$\frac{\partial \bar{c}}{\partial t} + \bar{w}_1 \frac{\partial \bar{c}}{\partial h} - \frac{\partial K}{\partial h}\frac{\partial \bar{c}}{\partial h} + \frac{\partial \bar{w}_1}{\partial h}\bar{c} = K\frac{\partial^2 \bar{c}}{\partial h^2} \tag{3}$$

The second term on the left-hand side of this equation is the usual advective term; the third term is a similar term due to the so called pseudo velocity, i.e. the vertical gradient of the diffusivity; and the fourth term represents dilution of the tracer concentration due to a vertical divergence of fluid, which is balanced by tracer-free water entering the averaging region.

The mean diapycnal velocity $\bar{w}_d$ can be related to the diffusivity K and to the input of solar radiation through the equation:

$$\bar{w}_d \frac{\partial \bar{\sigma}}{\partial h} = \frac{\partial}{\partial h}\left(K\frac{\partial \bar{\sigma}}{\partial h}\right) - \frac{\alpha}{C_p}\frac{\partial \bar{I}}{\partial h} \tag{4}$$

where $\partial\bar{\sigma}/\partial h$ is the area-averaged potential density gradient, α is the thermal expansion coefficient, C_p is the heat capacity of the water, and $\bar{I}$ is the mean downward flux of solar energy at height h. The left-hand side of Eq. (4) is the total time rate of change of potential density in isopycnal coordinates, since in those coordinates $\partial\bar{\sigma}/\partial t$ and the gradient of potential density along-isopycnal surfaces are both zero. The first term on the right is the contribution from mixing and the second term is the contribution from the absorption of solar energy flux. We assume in Eqs. (3) and (4) that the diffusivity K is the same for heat, salt and tracer. The effect on potential density of along-isopycnal mixing of heat and salt, i.e. cabelling, has been ignored.

The downward light flux $\bar{I}$ was computed from the equation:

$$\bar{I}(z) = 0.45 I_0\{a\exp(k_{w1}z + k_{chl}\int_0^z F(z)\mathrm{d}z) + (1-a)\exp(k_{w2}z)\} \tag{5}$$

I_0 is the 300–3000 nm radiation flux in W m^{-2} just below the sea surface, estimated from the ship's radiometer, adjusted for albedo as a function of solar angle and atmospheric transmission from Table 1 of Payne (1972), which is a tabulation of field data based on simultaneous upward- and downward-looking pyranometers above the sea surface. The factor 0.45 accounts for loss of the 700–3000 nm waveband in the upper meter of the water column. The remaining incident radiation (viz. PAR) is divided into two spectral bands: a fraction $a = 0.784$ in a short wavelength (400–625 nm) band with $k_{w1} = 0.0403\,\mathrm{m}^{-1}$ and $k_{chl} = 0.0397\,\mathrm{m}^2/\mathrm{mg}$, and the rest in a long wavelength (625–700 nm) band with $k_{w2} = 0.4154\,\mathrm{m}^{-1}$. $F(z)$ is an estimate of the concentration of chlorophyll plus phaeopigments from fluorescence as a function of depth (see Section 2.2). The values for a, k_{w1} and k_{chl} were determined by optimizing the fit of Eq. (5) to measurements of $I(z)$ from deck-mounted and Rosette-mounted PAR sensors and $F(z)$; these values agree reasonably with values in the literature (e.g. Morel and Maritorena, 2001; Oschlies and Garcon, 1999). The value of k_{w2} was computed from Morel and Maritorena's (2001) extinction

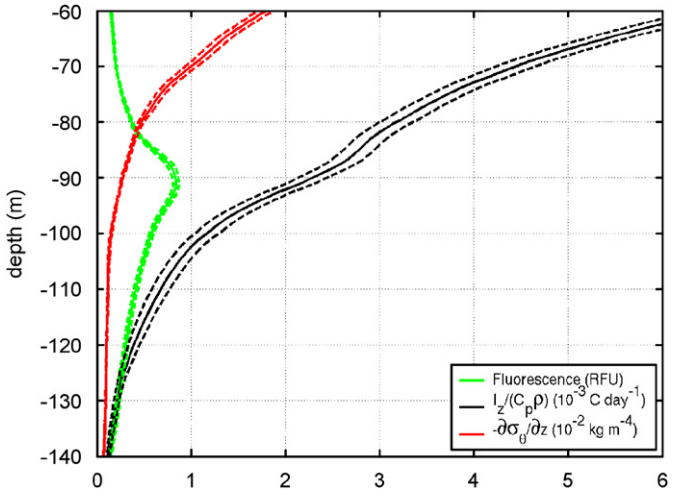

Fig. 12. Mean vertical profiles of fluorescence, heating rate, and density gradient for the period of the tracer release experiment. Means have been calculated as a function of density and transformed to depth using the mean isopycnal depth. The mean heating rate profile was estimated with the procedure described in the Section 4.1.

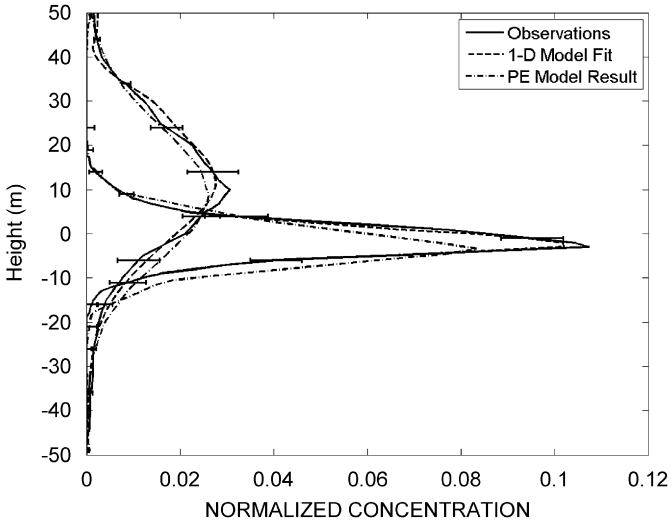

Fig. 13. Normalized mean tracer profiles (solid curves), and model fits. Height is relative to the target potential density surface. The dashed curves indicate the least squares fit for the 1-D advection–diffusion model described in Section 4, with $K = 3.5 \times 10^{-5}\,\mathrm{m^2/s}$. The dash-dot curves show the mean normalized profiles for the 3-D primitive equation model described in Section 5.

coefficients for a surface concentration of 0.05 mg Chl/m^3 assuming Neckel and Lab's spectrum (Bird and Riordan, 1986). A normalized heating rate was computed from the vertical divergence of the light field $\partial\bar{I}/\partial z$ for each $F(z)$ profile and averaged along isopycnals for each cruise; these estimates were then averaged in time using the observed $I_0(t)$. The result is shown in Fig. 12, along with the mean fluorescence profile, and the profile of the mean potential density gradient, which plays an important role in Eq. (4). Although the deep chlorophyll layer has a clear affect on the mean heating rate profile, it does not create a sign reversal in the gradient of that profile, a possibility illustrated by Lewis et al. (1983).

Eqs. (3) and (4) can be used with our measurements of the mean concentration profiles for the two surveys in a one-dimensional (1-D) advection–diffusion model to estimate K and its variation with h. A least-squares approach was taken, with a cost function constructed as described by Ledwell and Bratkovich (1995; their Eq. (8)) from the uncertainties in both the initial and final profiles, shown as error bars on the mean profiles in Figs. 6 and 8. All of the terms in Eqs. (3) and (4) are included in the analysis. The density and radiation profiles were allowed to vary linearly with time at each level h between mean profiles determined from all CTD casts made within 20 km of eddy center during the initial tracer cruise, the middle survey cruise and the final tracer cruise. The nominal times of the surveys are listed in Table 1. The best fit was found for $K = 3.5 \times 10^{-5}\,\mathrm{m^2/s}$ (uncertainty about $0.5 \times 10^{-5}\,\mathrm{m^2/s}$), and the modeled profiles are compared with the observed profiles in Fig. 13. Not only does this diffusivity give the observed broadening of the tracer distribution, but, when combined with solar heating, it also provides the observed rise of the tracer cloud relative to the target isopycnal surface through Eq. (4). The diffusive term and the radiative term on the right-hand side of Eq. (4) contribute about equally to the diapycnal velocity.

Variations in solar heating rate in different parts of the tracer patch can cause dispersion of the tracer in density space, and so can contribute to the apparent diapycnal diffusivity. We have estimated this contribution to be less than $0.5 \times 10^{-5}\,\mathrm{m^2/s}$ from the variance of the solar absorption expected from the variations in the fluorometer signal and depth at the $\sigma_\theta = 26.255\,\mathrm{kg/m^3}$ surface.

The best fit to the data was found with K independent of h and of time. However, a fit nearly as good was found by allowing K to increase linearly from 0 at $h = -50$ m to $5 \times 10^{-5}\,\mathrm{m^2/s}$ at $h = +50$ m. Thus, we cannot rule out the possibility, with the tracer observations, that K did not increase upwards. Also, a fit nearly as good was found with a diffusivity of $5.3 \times 10^{-5}\,\mathrm{m^2/s}$ between the initial tracer survey and the middle hydrographic survey centered around 17 August, a stormy period, and half this value between the middle hydrographic survey and the final tracer survey. Hence, we cannot rule out the possibility that the diffusivity was enhanced during the stormy period, and in fact this seems likely since it was during this period that the majority of the descent of isopycnal surfaces in the upper 80 m of the water column took place.

4.2. Vertical velocity

The rise of the tracer relative to the target density surface seen in Fig. 13 is due to solar heating and to convergence of buoyancy flux by mixing. The vertical velocity of the fluid, w, which is of great importance in the supply of nutrients to the euphotic zone, includes the motion of the isopycnal surfaces as well as flow across isopycnal surfaces. The total

vertical velocity is given by the equation:

$$w = u \cdot \nabla_\sigma z + \left[\frac{\partial z}{\partial t}\right]_\sigma + w_d$$
$$= u \cdot \nabla_\sigma z + \left[\frac{\partial z}{\partial t}\right]_\sigma + K\frac{\partial^2 \sigma}{\partial z^2}\left[\frac{\partial \sigma}{\partial z}\right]^{-1}$$
$$- \frac{\alpha}{C_p}\frac{\partial I}{\partial z}\left[\frac{\partial \sigma}{\partial z}\right]^{-1} + \frac{\partial K}{\partial z} \quad (6)$$

where u is the horizontal velocity vector, $\nabla_\sigma z$ is the slope of the isopycnal surface, and z is the vertical coordinate relative to the ocean surface, as opposed to h in Eqs. (1) and (4), which is relative to the isopycnal surface of the injection. Derivatives with respect to h are virtually the same as derivatives with respect to z, however. We have ignored the small angle between the normal to the isopycnal surface and the vertical in the diapycnal terms in Eq. (6). The first term, $u \cdot \nabla_\sigma z$, in Eq. (6) is the contribution to w from motion along sloping isopycnal surfaces. The second term represents the vertical motion of isopycnals. The other terms represent the velocity of the fluid relative to the isopycnal surfaces, and are from Eq. (4).

We shall argue in Section 5 that the first term on the right-hand side of Eq. (6) is much smaller than the others in the deep fluorescence layer. Estimates from the data of the middle three terms in this layer are shown in Fig. 14. The first of these terms, the velocity of the isopycnal surfaces, was about 0.1 m/d, estimated from changes with time in the mean density profile. The second term, due to diffusion, has a value of about 0.2 m/d, based on the density profiles with $K = 3.5 \times 10^{-5}\,m^2/s$. The third term, estimated from profiles of solar radiation and density, reached a peak of

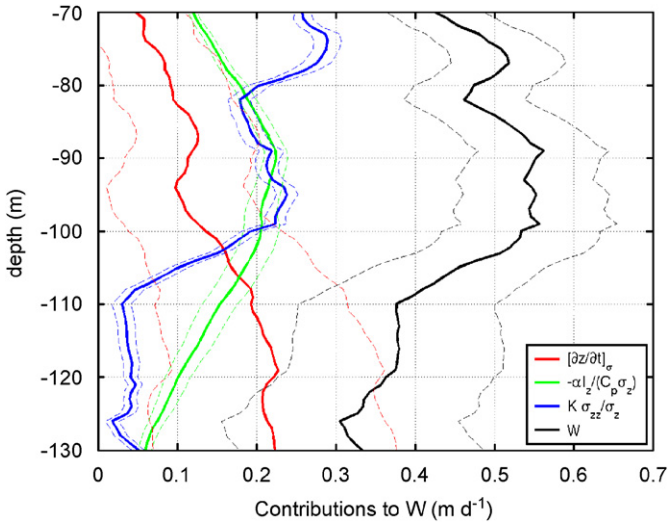

Fig. 14. Contributions to the vertical velocity from solar heating (green), from convergence of buoyancy flux due to mixing (blue), and from upward movement of the isopycnal surfaces (red), and the sum of these (black), for the inner 20 km of the eddy. These contributions are estimated as a function of density and then transformed to depth using the mean depth of the density surfaces for the period of the tracer experiment.

0.2 m/d near the chlorophyll maximum. The best fit diffusivity was constant with depth, but as noted earlier, a diffusivity that increases from 0 to $5 \times 10^{-5}\,m^2/s$ over 100 m cannot be ruled out. This gradient would contribute 0.04 m/d to the vertical velocity through the last term on the right-hand side of Eq. (6), and so would play a minor role, if any. The total vertical velocity is about 0.55 m/d, at the level of the tracer and the peak fluorescence, where it is most accurately determined (Fig. 14).

4.3. Along-isopycnal dispersion

The apparent evacuation of the tracer from the central 10 km of the eddy between injection and initial sampling is striking (Fig. 9). We also observed that in most cases a drogue or profiling float deployed near eddy center would be expelled from the central 10 km or so within a few days. The process involved is mysterious. It is much too fast to be due to an axially symmetric divergence from the center of the eddy, as the following argument shows. In an axially symmetric system the radial velocity of a particle dr/dt at radius r is given by the equation:

$$\frac{dr}{dt} = -\frac{r}{2}\frac{\partial w}{\partial z} \quad (7)$$

If the divergence of the vertical velocity is roughly independent of r, with a value γ, then the solution to this equation is

$$r = r_0 \exp(-\gamma t/2) \quad (8)$$

where r_0 is the initial distance from eddy center. For negative γ, i.e. a convergent w, the distance from center would grow exponentially. For particles to start at $r_0 =$ 3 km and move to 10 km after 8 days, as suggested by the behavior of the tracer between the injection and the first survey (Fig. 9), and by the drifters, a value of $\gamma = -(2/t)\ln(r/r_0) = -0.3\,d^{-1}$ would be required. This means that w would have to decrease by 6 m/d over 20 m, for example, for a mean vertical convergence to be responsible for the radial divergence observed in the tracer. A vertical convergence this large could not be due to diapycnal processes, as shown in the previous section, and would have appeared clearly as dramatic displacements of isopycnal surfaces relative to one another. Thus, this axisymmetric process must be ruled out.

If tracer and drifters are expelled from the center of the eddy, then it must be by motions that are not axially symmetric, perhaps associated with an instability wherein fluid rushes into eddy center from one direction while a stream of fluid exits in another. It is perhaps surprising that the tracer was not stirred back into the central region during the course of the experiment, but note that even at the time of the final survey (Fig. 7) there appear to be azimuthal sectors that are poor in tracer from which fluid mixing toward the center might have been drawn. The time and length scales of the experiment may not be very different from those of the isopycnal mixing events

themselves, and hence the center in our case remained relatively free of tracer.

Strong radial dispersion continued between the initial and final surveys, as seen in Fig. 9. An along-isopycnal diffusivity can be estimated crudely at 20-km scale from the growth of the second moment of the tracer distribution between the injection and the final survey, discussed in Section 3.3. For Fickian diffusion, we would have $K_H = \Delta\langle r^2\rangle/2\Delta t$, where $\Delta\langle r^2\rangle = (455–181)\,\mathrm{km}^2$ is the growth of the mean square radius, and $\Delta t = 44$ days is the elapsed time. The resulting estimate for K_H is a little less than $40\,\mathrm{m}^2/\mathrm{s}$, which is rather large. For example, a value of $2\,\mathrm{m}^2/\mathrm{s}$ was estimated for dispersion at scales of 1–30 km at 300 m depth in the eastern subtropical Atlantic by Ledwell et al. (1998), while a value of $22\,\mathrm{m}^2/\mathrm{s}$ was inferred from the dispersion of tracer in the mixed layer within an anticyclonic mode-water eddy in the northeast Atlantic at scales similar to those in the present case by Martin et al. (2001). This large diffusivity suggests strong submesoscale mixing near eddy center. The isopycnal diffusivity is certainly scale-dependent, and probably depends on distance from eddy center. Our estimate for K_H applies to length scales of 10 or 20 km, within the inner 40 km of the eddy and will be used to estimate the flux of nutrients into the center of the eddy by isopycnal mixing in the next section.

4.4. Flux of dissolved inorganic nitrogen (DIN)

Profiles of DIN were obtained from many of the CTD casts during the three cruises. The profiles taken within 20 km of eddy center have been averaged on density surfaces, and then plotted versus depth, along with fluorescence, using the mean isopycnal depth from the period of the tracer experiment (Figs. 4B and 15). In these coordinates DIN was less than $0.02\,\mathrm{mmol/m}^3$ on isopycnal surfaces whose mean depth was less than 70 m. DIN rose steeply with depth in the layer of the fluorescence maximum, and was greater than $1\,\mathrm{mmol/m}^3$ below 105 m depth. Thus, the depth interval of steepest DIN gradient was approximately coincident with the fluorescence maximum, as would be expected if plankton in that zone were consuming DIN.

The vertical flux of DIN, ϕ_N, is given by the equation:

$$\phi_N = w[\mathrm{DIN}] - K\frac{\partial[\mathrm{DIN}]}{\partial z} \tag{9}$$

where w is the vertical velocity discussed in Section 4.2, and K is the diapycnal diffusivity estimated in Section 4.1. Contributions to ϕ_N from these two terms are shown in Fig. 15 as a function of depth. The sum of these contributions was approximately constant at $0.60\pm 0.1\,\mathrm{mmol/m}^2/\mathrm{d}$ between 130 and 100 m depth, above which it declined toward zero at 70 m due to uptake by phytoplankton in the patch of high fluorescence.

We have not included the contribution to w from mean flow along sloping isopycnal surfaces in this estimate, represented by the first term on the right-hand side of

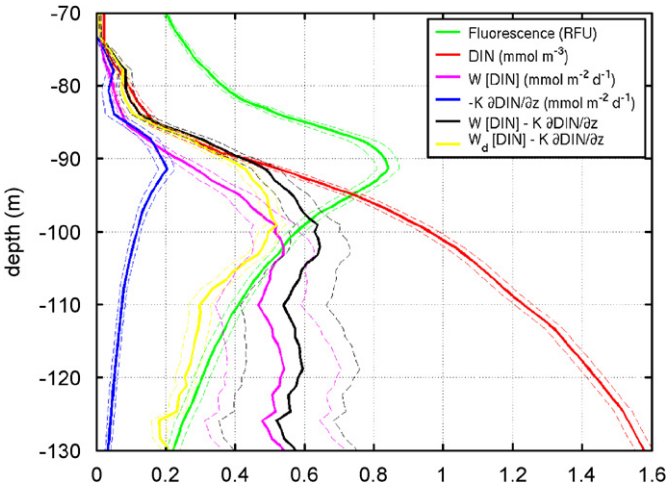

Fig. 15. Mean profiles of fluorescence (green), DIN (red), total DIN flux (black) and the contributions to DIN flux from eddy diffusion (blue) and from advection (magenta). The yellow line shows the total DIN flux relative to isopycnal surfaces. The light dashed lines show estimates of the uncertainty in each curve.

Eq. (6), or from isopycnal mixing. For the axially symmetric system we have here, in the mean, the contribution from the former would be (see Eq. (7))

$$u\cdot\nabla_\sigma z = -\frac{r}{2}\frac{\partial w}{\partial z}\left(\frac{\partial z}{\partial r}\right)_\sigma \tag{10}$$

where r is the radial coordinate. Fig. 14 shows an increase in the vertical velocity of about 0.17 m/d between 110 and 90 m depth, i.e. just below the chlorophyll maximum, though with large uncertainty. This divergence is 40 times smaller in magnitude than the divergence required to expel the tracer from the inner 10 km with axisymmtric flow, as estimated in the previous section, and it is of the opposite sign. A smaller divergence, on the order of 0.01 m/d over these 20 m, is expected for upwelling driven by wind-stress curl at the surface, as shown by the primitive equation model presented in Section 5.1. The slope of the $\sigma_\theta = 26.255\,\mathrm{kg/m}^3$ isopycnal surface, estimated from the CTD sections obtained on OC415-3, was on the order of 0.001 at 20-km radius, decreasing to zero within about 10 km of eddy center. Even if we take the vertical divergence from Fig. 14, the vertical velocity due to mean flow along-isopycnal surfaces at $r = 20$ km would be $+0.08$ m/d, so just 15% of the sum of the other terms in Eq. (6), and it would decrease toward the center.

Flux of nutrients into the center of the eddy by isopycnal stirring is also likely to be positive, since DIN is depleted on isopycnal surfaces near eddy center (Fig. 16), but this contribution also would have been relatively small. The total radial diffusive flux per unit of depth at radius r, $\phi_H(r)$, is given by

$$\phi_H(r) = -2\pi r K_H\frac{\partial[\mathrm{DIN}]}{\partial r} \tag{11}$$

where K_H is the isopycnal diffusivity. We estimated in the previous section a value for K_H of approximately $40\,\mathrm{m}^2/\mathrm{s}$.

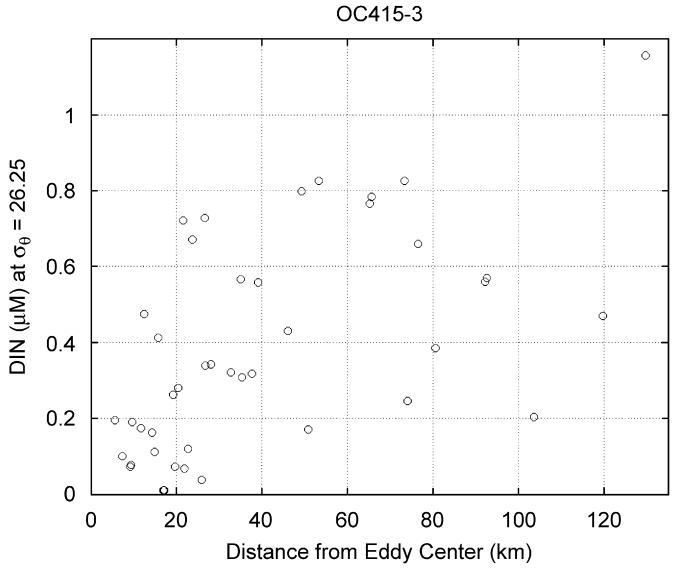

Fig. 16. DIN from bottle samples interpolated to $\sigma_\theta = 26.25$ during OC415-3, between the two tracer cruises, as a function of distance from eddy center.

The radial gradient of [DIN] is on the order of 0.5 μM over 50 km, estimated from the scatter plot shown in Fig. 16. To compare the along-isopycnal flux with the vertical flux at 100 m, consider the ratio of $h\phi_H$ to $\pi r^2 \phi_N$, where $h = 20$ m is the thickness of the nitracline layer above 100 m. This ratio, with the values given here and with $\phi_N = 0.6$ mmol/m^2/d, is on the order of 0.15. Hence, the flux of 0.6 mmol/m^2/d estimated above may have been enhanced by a factor of ~15% for both isopycnal advection and isopycnal diffusion.

Not all of the nutrients entering the euphotic zone were consumed during the period of the experiment. Rather, the inventory of DIN increased at all levels near eddy center, especially between OC415-3 and OC415-4 (Fig. 17C). We have estimated the inventories above 100 m for each cruise. Comparing the increase in inventory between 65 and 100 m with the flux from Fig. 15 at 100 m, we find that about 40% of the DIN that flowed upward over the 36 days between the initial and final tracer surveys remained unconsumed at the time of OC415-4. Hence, the consumption rate for DIN in the euphotic zone that we estimate for the period from

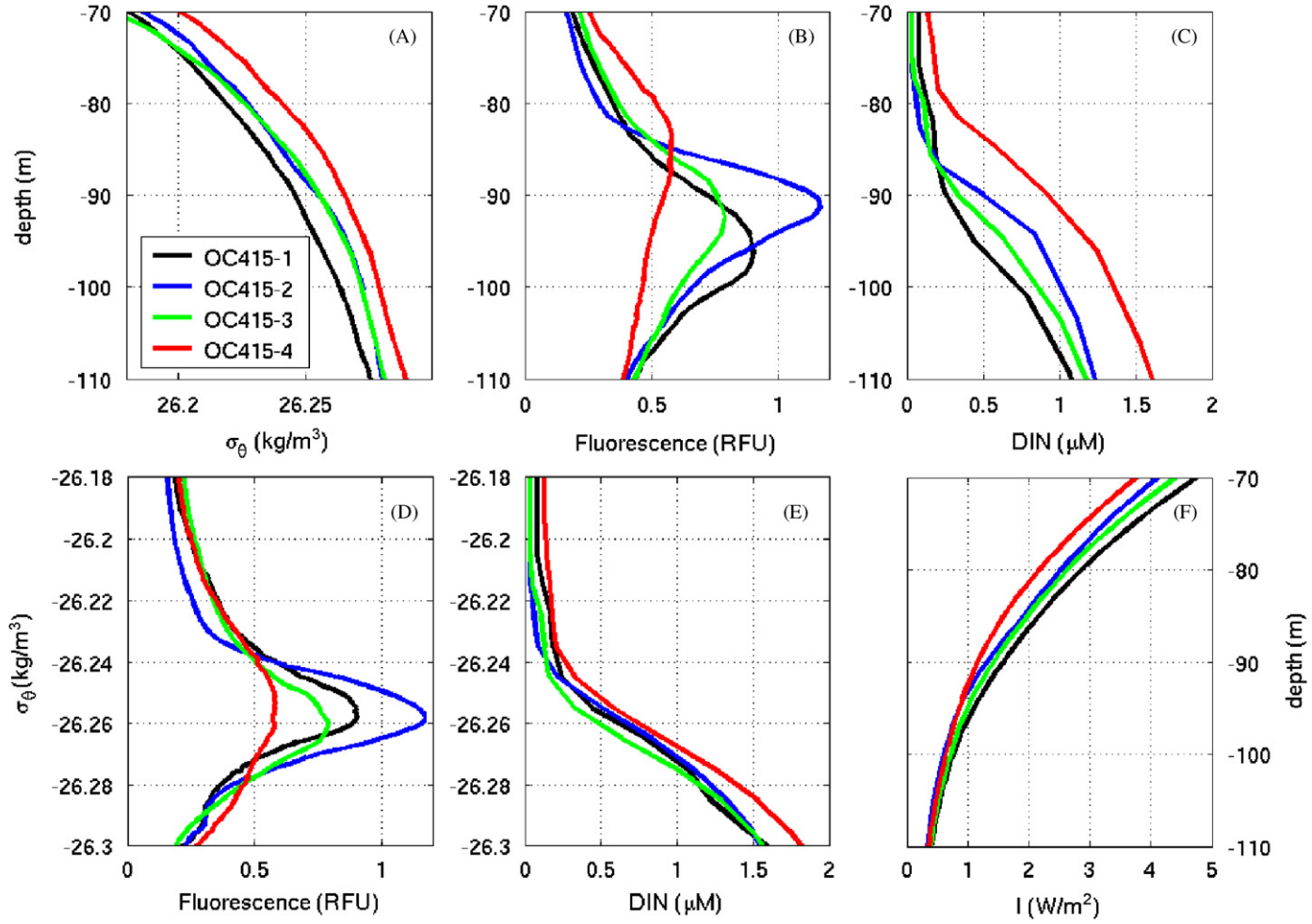

Fig. 17. Mean density (A), fluorescence (B), DIN (C), and downward radiation flux I (f), as a function of depth for the four Oceanus cruises in 2005. Panels (D) and (E) show the fluorescence and DIN as a function of potential density.

31 July to 5 September is 0.27 mmol/m^2/d. This estimate is a bit larger than estimates from the mean downward flux of 0.16 mmol/m^2/d of particulate organic nitrogen caught by sediment traps at 150 m depth in the core of the eddy (Buesseler et al., 2008). Our estimate would err slightly on the low side if contributions to the flux from isopycnal advection and diffusion discussed above are present.

The fluorescence maximum, isopleths of DIN, isopycnals, and isolumes all shoaled during the experiment in subtle relation to one another (Fig. 17). The fluorescence peak and nitracline shoaled about 7 m during the tracer experiment (OC415-2 to OC415-4 in Fig. 17B), but both the fluorescence peak and the nitracline remained approximately fixed in density coordinates (Fig. 17D and E), since isopycnal surfaces shoaled by about 6 m (Fig. 17A). Since the tracer moved upward by 12 m relative to the density surfaces, neither fluorescence nor DIN behaved like the passive tracer. It appears that as summer progressed nutrients were consumed by the plankton, tending to hold the nitracline deep relative to the upwelling water, so that it happened to stay nearly fixed in density coordinates. The phytoplankton patch associated with the fluorescence stayed with the nitracline, and therefore also remained nearly fixed in density coordinates. The 1 W/m^2 isolume also shoaled during the tracer experiment, but by less than 3 m (Figs. 17F). Changes in cloud cover compensated for much of the seasonal decrease in solar elevation and length of day. For some purposes it may be of interest to know the flux of nutrients relative to these various isopleths, and in those cases the motion of the isopleths must be subtracted from that of the nutrients. Our estimates of DIN flux at fixed depth seem to us, however, to be the appropriate fluxes for the euphotic zone, because of the relative stationarity of the 1 W/m^2 isolume.

4.5. Forcing of the vertical velocity

We have shown in Section 4.2 that the vertical velocity in the vicinity of the deep chlorophyll layer was around 0.55 m/d during the 36-day tracer experiment. This upwelling was most likely driven by the curl of the wind stress associated with the rotation of the eddy, as suggested by simple models (Dewar and Flierl, 1987; Martin and Richards, 2001). The stress is greater on the side of the eddy where the current opposes the wind. For an anticyclonic eddy, this wind-stress curl drives a divergence of water from eddy center, which must be balanced by an upward flux from below. Applying the model of Martin and Richards (2001), and using QuikSCAT winds (Fig. 18) and surface velocities derived from ADCP data, we find that the average upwelling velocity in the 20-km core of Eddy A4 was approximately 0.42 m/d at the base of the Ekman Layer, about 25% less than our estimate of the vertical velocity in the layer occupied by the tracer. We suspect that the wind stress may have been underestimated from the 12-h QuickSCAT winds and bulk formulae during the storms that dominate the record, and so we take this as support for the theory.

The question arises of how far below the base of the Ekman layer uplift driven by the wind-stress curl is felt. The depth scale is set by a competition between the stratification, which resists upward motion, and rotation, which resists the horizontal convergence required to balance a divergence in the vertical velocity. The convergence

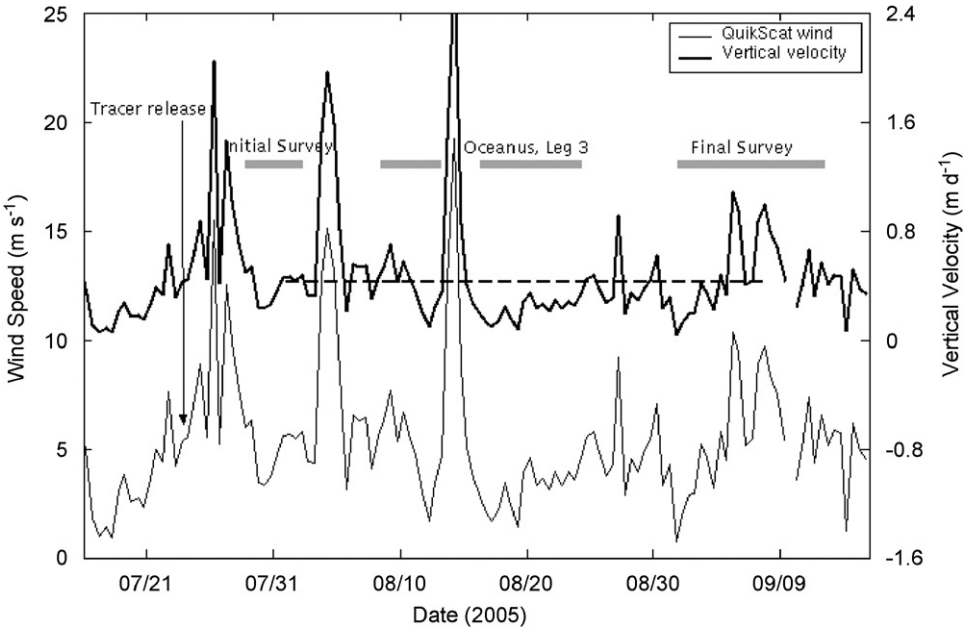

Fig. 18. Wind record from QuickSCAT and estimated vertical velocity, averaged over the inner 20 km, induced by the wind stress curl during the tracer release experiment. The times of the tracer release,of the initial and final tracer surveys, and of the intervening survey (Oceanus, Leg 3, interrupted by a storm) are indicted. The dashed line is drawn at the average vertical velocity for the period, 0.28 m/d. Note the tropical storms in late July and early August.

cannot be so great that the azimuthal flow demanded by conservation of potential vorticity becomes out of geostrophic/cyclostrophic balance with the density field. Quasigeostrophic theory indicates that the upwelling diminishes with depth in the seasonal pycnocline with a vertical scale of fL/N, where f is the Coriolis frequency, as modified by the rotation of the eddy, N is a buoyancy frequency characterizing the seasonal pycnocline, and L is the horizontal length scale of the eddy (see Appendix A). This vertical scale is on the order of 250 m for the seasonal pycnocline in eddy A4. Hence, the vertical velocity measured at the level of the tracer release could well be driven by the wind-stress gradient across the eddy. We examine this mechanism more quantitatively in the next section with a 3-D numerical model.

5. Numerical model

5.1. Modeling methods

A numerical model of the dynamics of the eddy was developed to estimate the wind-driven upwelling at the base of the euphotic zone. The model is based on the Los Alamos Parallel Ocean Program (POP), a level-coordinate model that solves the 3-D primitive equations with a free surface (Smith et al., 1992, 2000). An isolated eddy with characteristics of A4 is simulated in a 500 km × 500 km doubly periodic domain with 2.88 km horizontal resolution. The vertical grid consists of 72 levels, with spacing increasing gradually from 5 m at the surface to 125 m at depth, and with the bottom at 4462 m depth. Tracers are advected using a centered-difference scheme (MPDCD) with a flux limiter to maintain positive definite concentrations (Oschlies and Garcon, 1999; McGillicuddy et al., 2003). Horizontal mixing utilizes a Laplacian operator with diffusivity and viscosity of 1 m^2/s. This explicit diffusivity is small compared with the isopycnal diffusivity estimated in Section 4.2 to avoid artificial diapycnal mixing due to horizontal mixing across sloping density surfaces. Vertical mixing is implemented using the K-profile method (Large et al., 1994) with a background diffusivity of 3.5×10^{-5} m^2/s in accordance with the diffusivity estimated in Section 4.1 from vertical spreading of the tracer. The model is configured on an f-plane (centered at 30°N) so that the simulated eddy stays in the center of the model domain, greatly simplifying computational diagnostics in eddy coordinates.

Initial temperature and salinity distributions are fit to hydrographic data from eddy A4 assuming radial symmetry:

$$T(r,z) = T_{\text{out}}(z) + (T_{\text{in}}(z) - T_{\text{out}}(z))\exp(-r^2/r_o^2) \quad (12a)$$

$$S(r,z) = S_{\text{out}}(z) + (S_{\text{in}}(z) - S_{\text{out}}(z))\exp(-r^2/r_o^2) \quad (12b)$$

where T_{in}, T_{out}, S_{in} and S_{out} are inside and outside temperature and salinity profiles from CTD data, r is radius from eddy center, and z is depth. The scale $r_o = 83$ km provides a least-squares fit to hydrographic data in cross section, with downward (upward) displacement of the main (seasonal) pycnocline characteristic of a mode-water eddy (Fig. 19). The baroclinic velocity is computed from the density field, assuming geostrophic and cyclostrophic balance with no motion in the lowermost level. A barotropic velocity proportional to the baroclinic velocity was added to bring the peak total velocity to 30 cm/s, in accord with observations from ADCP surveys of A4. The azimuthal velocity increases linearly with radius in the core of the eddy (solid-body rotation), reaches a maximum at a radius of 59 km, and decays exponentially outside (Fig. 19D). Depression of the main pycnocline results in anticyclonic motion, although reversal of geostrophic shear

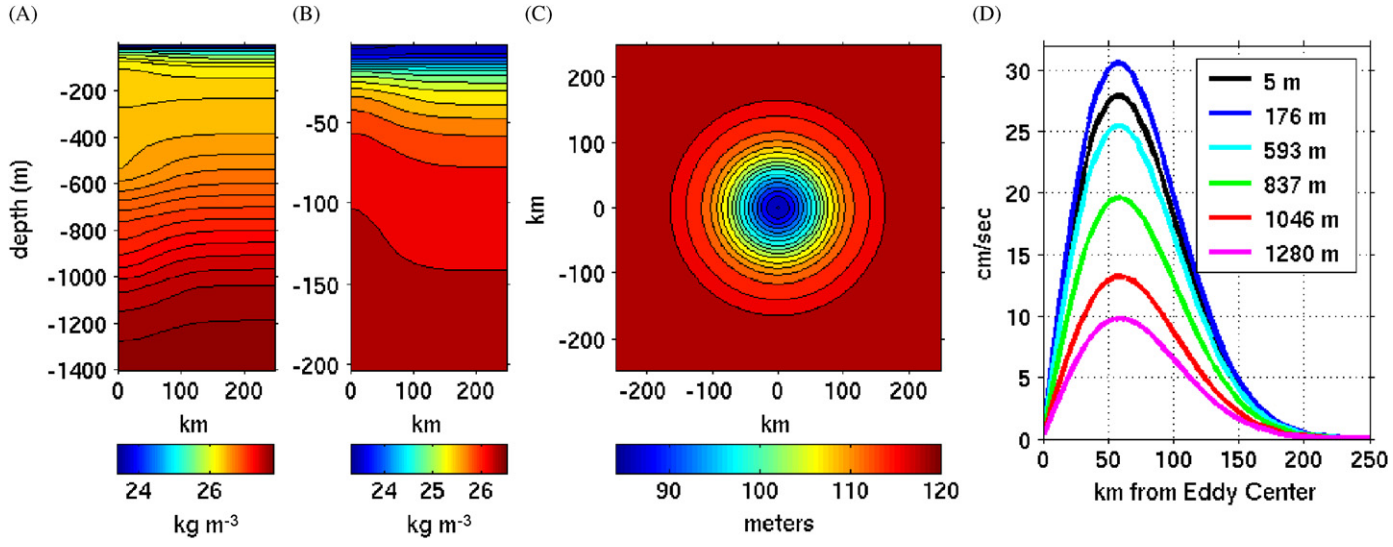

Fig. 19. Model initial conditions for July 20: (A) potential density anomaly, 0–1400 m (σ_θ (r,z)); (B) potential density anomaly, 0–200 m (σ_θ (r,z)); (C) horizontal (x–y) map of the depth of the 26.27 isopycnal (depth of $\sigma_\theta = 26.27$); (D) azimuthal velocity at various depths.

associated with doming of the seasonal pycnocline causes a subsurface maximum in velocity at 176 m depth.

A set of numerical experiments (Table 3) was designed to illustrate the physical processes responsible for the observed evolution of the tracer. These runs differ only in their surface forcing (see below). All runs are initialized on 20 July 2005. Each solution is allowed to adjust dynamically until 31 July, when 11 moles of tracer are distributed as found during the initial tracer survey, centered at 86 m (model level 16; $\sigma_\theta = 26.265\,kg/m^3$—chosen to be at about the same depth in the model as the actual tracer release was in the field, at $\sigma_\theta = 26.255\,kg/m^3$) in the inner 20 km of the eddy (Fig. 20A and F). The simulations are then run forward 36 days to the tracer-weighted time of the final tracer observations (September 5).

Runs 1–3 quantify the effect of wind stress, with an unforced case (Run 1), uniform stress (Run 2), and a stress dependent on the difference between air and sea velocities (Run 3), as in Dewar and Flierl (1987) and Martin and Richards (2001). The latter two runs are forced with a constant wind of 6.725 m/s, yielding a stress consistent with the mean observed surface stress for the period 20 July–12 September 2005 over Eddy A4 computed from QuikSCAT level 3 data (see http://podaac.jpl.nasa.gov/quikscat/). In these simulations with constant wind speed, the wind direction rotates through a complete circle every 64 h in order to avoid unrealistically persistent Ekman transport. Heat flux is added in Run 4, with a shortwave heat flux of 241 W/m^2 penetrating the sea surface (mean of shipboard data, minus a computed 4% albedo); bulk formulae are used to compute sensible, latent and longwave heat fluxes, following Doney (1996).

Table 3
Surface forcing in numerical experiments 1–4 (see text)

Run	Wind (m/s)	Wind stress formula	Heat flux
1	0	–	N
2	6.7	$\rho_a c_d U_a^2$	N
3	6.7	$\rho_a c_d (U_a - U_o)^2$	N
4	6.7	$\rho_a c_d (U_a - U_o)^2$	Y

In the wind stress formula, ρ_a is the air density, c_d the drag coefficient, U_a the air velocity and U_o the ocean surface velocity.

5.2. Model results

In the absence of external forcing (Run 1) there is no vertical velocity and the tracer simply spreads vertically and radially (Fig. 20). The tracer term balance is primarily diffusive, with vertical mixing spreading the tracer both upward and downward, and lateral mixing spreading the tracer outward (Fig. 21). Although the vertical velocity is essentially zero, the mean density profile evolves under the influence of vertical mixing (Fig. 22, sixth column). This tends to deepen isopycnals in the upper 120 m, with mixing manifested as a diapycnal velocity w_d in the density equation. The horizontally integrated SF_6 maximum persists at 86 m (Fig. 23A), yet it rises slightly in density space (Fig. 23B) because vertical mixing has decreased the density at which the tracer maximum resides.

With uniform wind stress (Run 2), the final distribution of SF_6 is nearly the same as in the unforced case (Figs. 20 and 23). Again the diffusive fluxes dominate the tracer term balances, yet there is a noticeable signal in the advective terms (Fig. 21). A weak ($w < 0.05$ m/d) submesoscale overturning cell occurs in the model, with upwelling near eddy center and downwelling in a radial band just outside the inner core (Fig. 22). The tracer upwelled by this

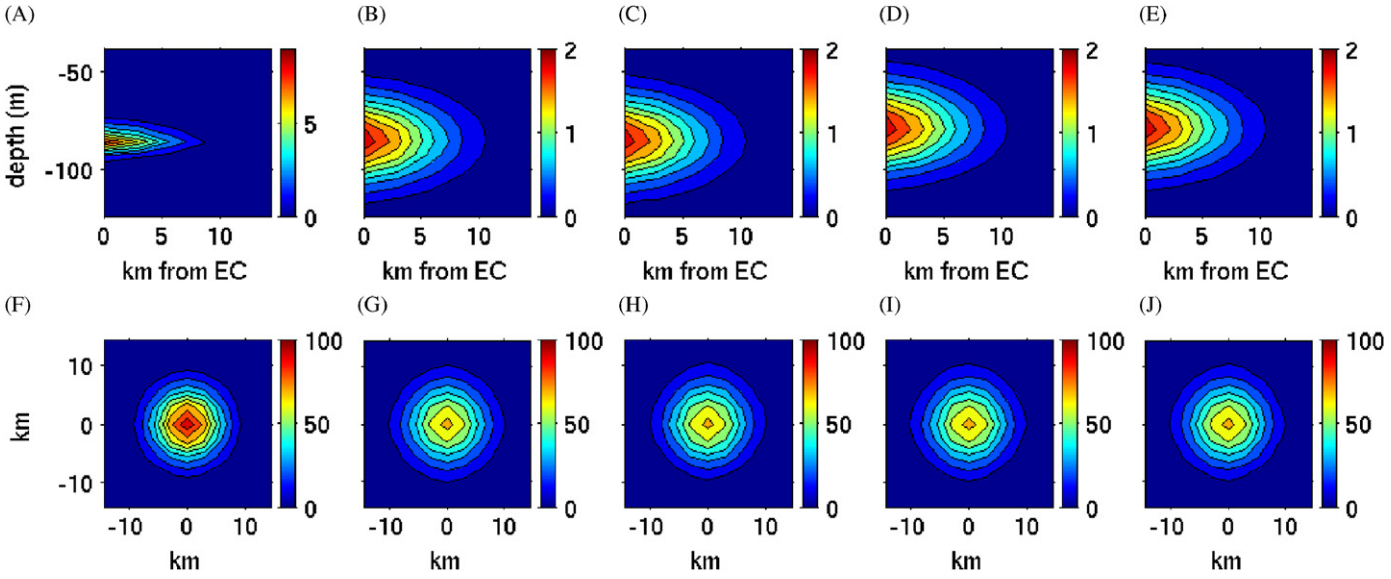

Fig. 20. Plan views and vertical cross-sections of SF_6 tracer for simulations 1–4: (A) Radially-averaged tracer on July 31; contour interval is 0.5 $nmol/m^3$. (B–E) Radially averaged tracer on September 5 in Runs 1–4; contour interval is 0.2 $nmol/m^3$. (F) Plan view of vertically-integrated tracer on July 31; contour interval is 10 $nmol/m^2$. (G–J) Plan view of vertically-integrated tracer on September 5 in Runs 1–4; contour interval is 10 $nmol/m^2$. Note that the radial sections (panels A–E) are not volume conserving; concentrations must be scaled with radius to visualize volumetric integrals.

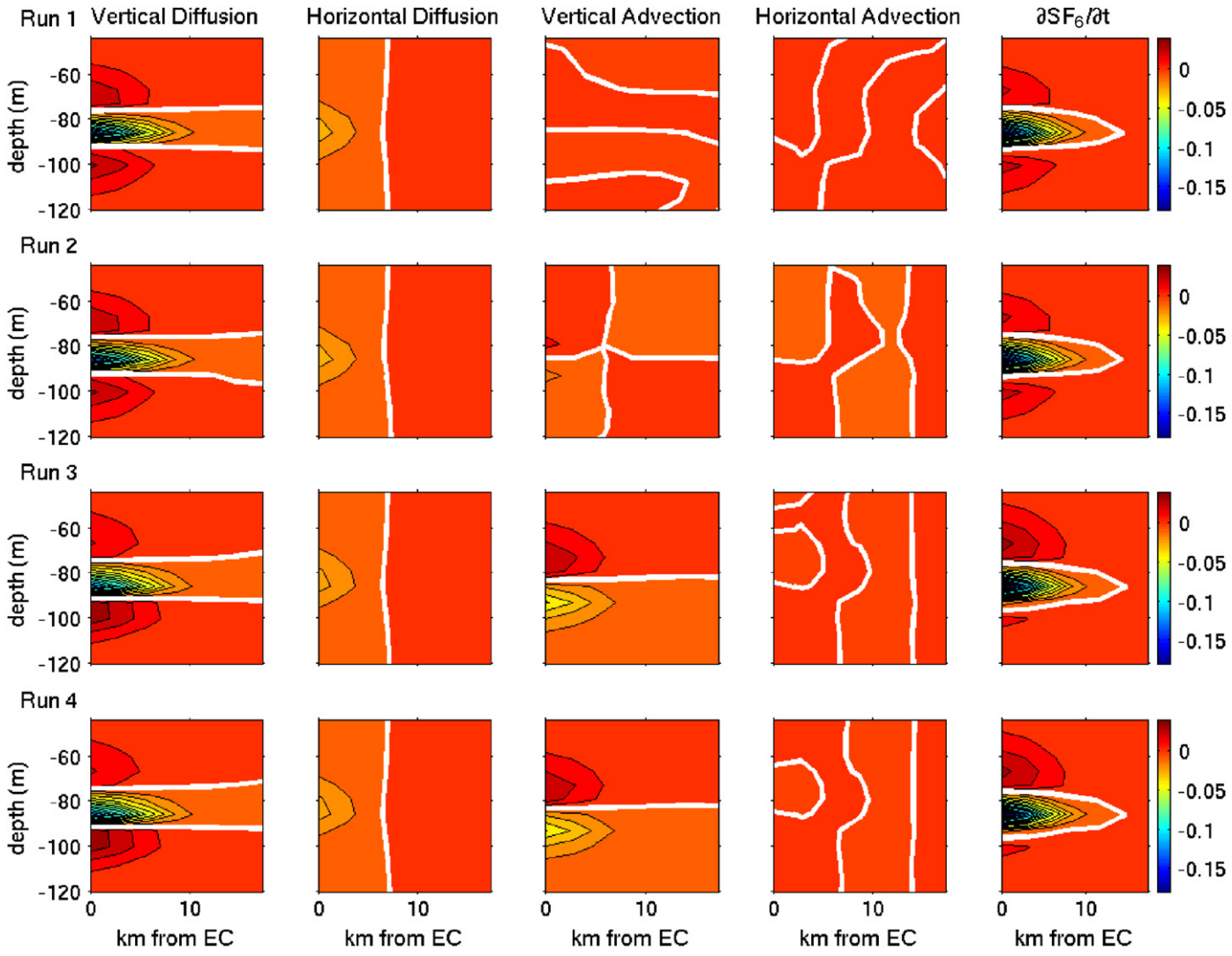

Fig. 21. Radially averaged tracer flux divergences (nmol/m^3/day) diagnosed from the advection–diffusion equation in Runs 1–4. The sign convention is such that the time rate of change (rightmost panel) is the sum of the other four terms. The contour interval is 0.01 nmol/m^3/day, and the thick white line is the zero contour. The horizontal axis is kilometers from eddy center (EC). Note that these radial sections are not volume conserving; diagnostics must be scaled with radius to visualize volumetric integrals.

secondary circulation is advected horizontally and downwelled, such that the horizontal and vertical advection terms are mirror images of each other, and no net vertical transport occurs (Fig. 21). Thus Runs 1 and 2 are essentially indistinguishable from each other in terms of the mean tracer profiles (Fig. 23).

When the surface current is accounted for in the wind-stress calculation (Run 3), substantial vertical motion is induced, with upwelling in the eddy interior and downwelling outside of it (Fig. 22). The maximum upwelling velocity of 0.23 m/d occurs at eddy center at the base of the Ekman layer, and penetrates down to the main thermocline. The upwelling is slightly weaker than estimated from the observed wind and currents in Section 4.4, partly because the radial gradient of the azimuthal velocity in the model is not as great as the observed gradient. Also, it is about half as great as the observed vertical velocity in the layer occupied by the tracer. This wind-driven upwelling causes vertical advection to become a primary player in the tracer term balance (Fig. 21). The SF_6 maximum shoals 6.7 m over the course of the simulation (Fig. 23, left panel), yet its position in density space is identical to the prior run (Fig. 23, right panel) because upwelling induced by this eddy/wind interaction is primarily isopycnal (Fig. 22).

Inclusion of solar heating (Run 4) causes the near-surface isopycnals to deepen (Fig. 22, sixth column), transforming the signature of the eddy/wind induced upwelling from primarily isopycnal to primarily diapycnal (cf. Fig. 22, bottom row). The final tracer distribution relative to the target isopycnal surface (Fig. 23B) is very similar to that observed and to the 1-D fit (Fig. 13), as it should be since the same diapycnal diffusivity from the 1-D fit was used in the 3-D model and the same radiation profile was used in both cases.

The model shows that the wind-driven upwelling is felt in nearly full force at the base of the euphotic zone, and in

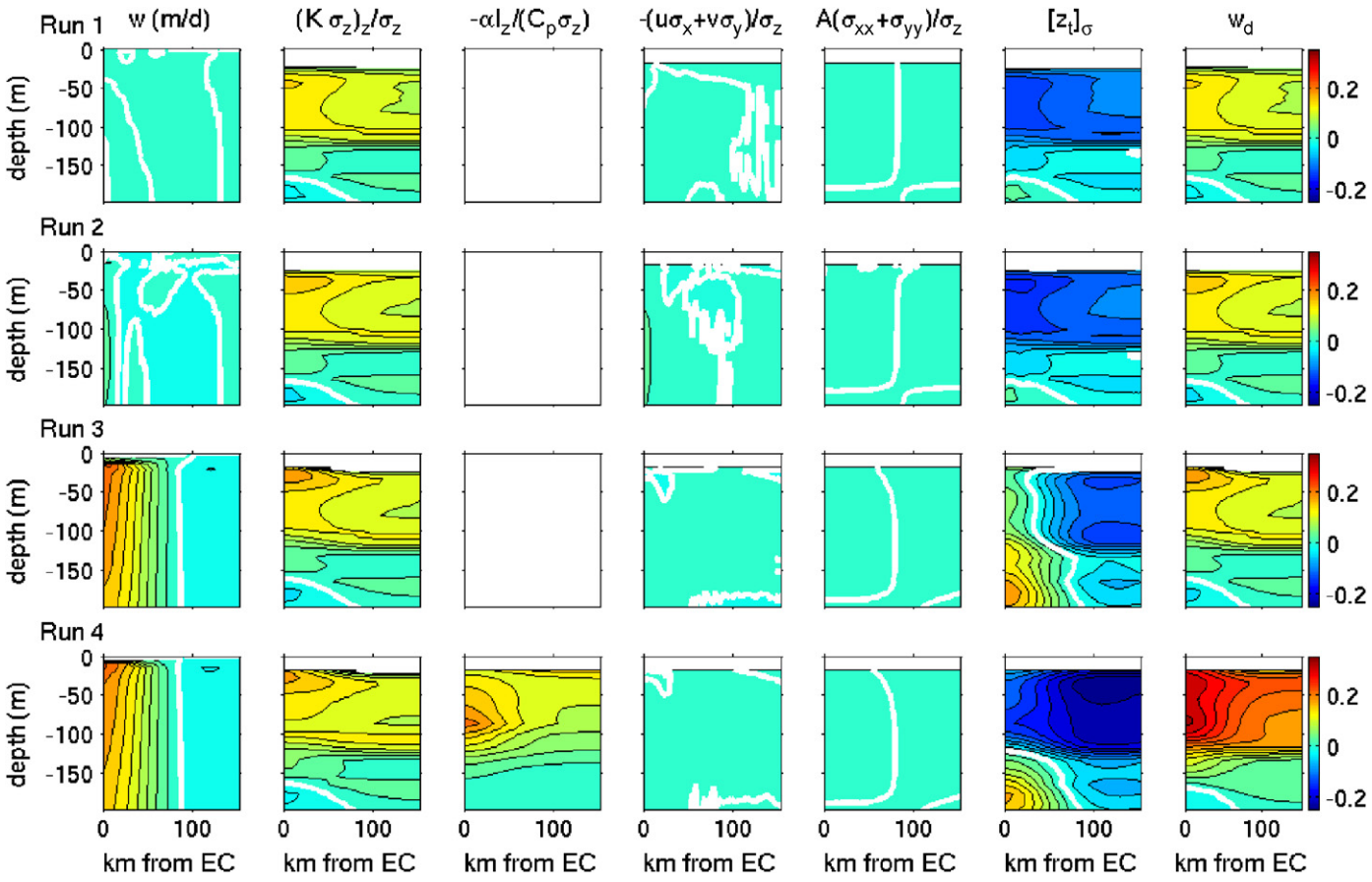

Fig. 22. Radially-averaged vertical velocity, w, and terms contributing to it for model runs 1 through 4. The contour interval is 0.025 m/d[1], and the thick white line is the zero contour. The second and third columns represent diapycnal terms on the RHS of Eq. (6). The fourth column represents advection along sloping isopycnals. The fifth column shows that the buoyancy source due to horizontal mixing in the model is negligible. The sixth column represents the vertical movement of the isopycnal surfaces. The last column, w_d, is the diapycnal velocity and is the sum of columns 2, 3 and 5. The third column is blank for Runs 1 through 3 in which there was no heating ($I_z = 0$). Also the terms (except w) are blank in the mixed layer where $\sigma_z \approx 0$. Note that these radial sections are not volume conserving; diagnostics must be scaled with radius to visualize volumetric integrals.

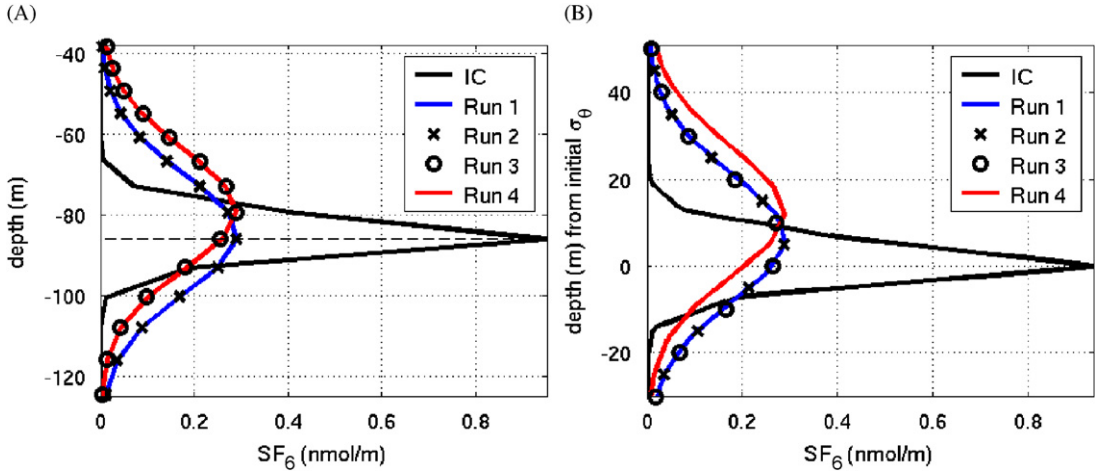

Fig. 23. Profiles of simulated tracer concentration inside the eddy in the initial condition (IC) and at the time of the final tracer survey (September 5): (A) horizontally integrated tracer plotted in depth coordinates; (B) isopycnally integrated tracer plotted as a function of vertical distance from the isopycnal of the injection.

fact penetrates into the weakly stratified layers below. It also illustrates how the vertical motion of a passive tracer is partitioned into diapycnal and adiabatic components. We conclude that the observed upwelling is driven primarily by eddy/wind interactions, while solar heating and diapycnal mixing provide buoyancy sources, enabling the upwelling

to be largely in the form of flow through the isopycnal surfaces rather than upward motion of the isopycnal surfaces.

6. Discussion

6.1. Mixing

The diapycnal diffusivity of $3.5 \times 10^{-5}\,m^2/s$ found from the tracer dispersion agrees well with estimates based on microstructure measurements near the base of the seasonal pycnocline in the eastern subtropical Atlantic (Lewis et al., 1986). This value is relatively high compared with the diffusivity of $5 \times 10^{-6}\,m^2/s$ believed to prevail in the background internal wave field of the stratified ocean (Gregg, 1989; Polzin et al., 1995). The diffusivity may have been enhanced by inertial waves generated by several storms passing over the eddy during the tracer experiment (Fig. 18). Furthermore, depression of the total vorticity within the eddy may have led to trapping of inertial waves (e.g., Kunze, 1985). The relative vorticity in the inner 20 km of the eddy was $-0.3\,f$, where f is the Coriolis frequency. The energy of waves generated with frequency between 0.7 f and f would be trapped and forced to dissipate locally, enhancing the diffusivity.

Data gathered from the hull-mounted ADCP during transects across Eddy A4 show that shear was enhanced near eddy center in the upper 40 m during OC415-1 (Fig. 24). In fact, Greenan (2008) has shown there to be a strong correlation between the shipboard ADCP shear and proximity to eddy center for all four cruises. The noise level of the ADCP shear was too great to see an enhancement at greater depths, if indeed there was any. Shear propagating downward to the depth of the chlorophyll maximum over a period of days after the passage of a storm was observed from profiling floats deployed by J. Girton near eddy center (personal communication). His observations did not include the outer part of the eddy, so they do not provide a contrast between inside and outside the features. Hence, our observations do not enable us to test whether internal wave shear was enhanced, or the gradient Richardson number was reduced, within the patch of high fluorescence relative to ambient waters.

Although the turbulent diffusivity measured with the tracer was large compared with current expectations for the pycnocline, the peak diffusive flux (Fig. 15) was an order of magnitude smaller than that necessary to support summertime annual new production of $1.5\,mmol\,N/m^2/d$ estimated for the North Atlantic subtropical gyre (e.g., Jenkins and Goldman, 1985). Furthermore, the diffusivity we observed is for a particularly stormy period and for the center of an anticyclonic eddy, where one might expect mixing to be enhanced by shear from trapped near-inertial waves. Hence, the experiment adds evidence that diapycnal mixing is not the main mechanism by which nutrients are provided to the euphotic zone in summer.

6.2. Wind–eddy interactions

It was recognized long ago that superposition of a wind-driven flow on oceanic fronts and eddies can lead to significant vertical transports (Stern, 1965; Niiler, 1969). Subsequent investigations revealed that mesoscale ocean currents create spatial variations in the surface stress itself (Dewar and Flierl, 1987; Martin and Richards, 2001), introducing yet another class of vertical transport processes. Up to now, these theoretical predictions have not been tested directly by measurements in the field. The tracer release experiment described here supports wind–eddy interactions as the primary cause of sustained upwelling in the interior of an anticyclonic eddy. The

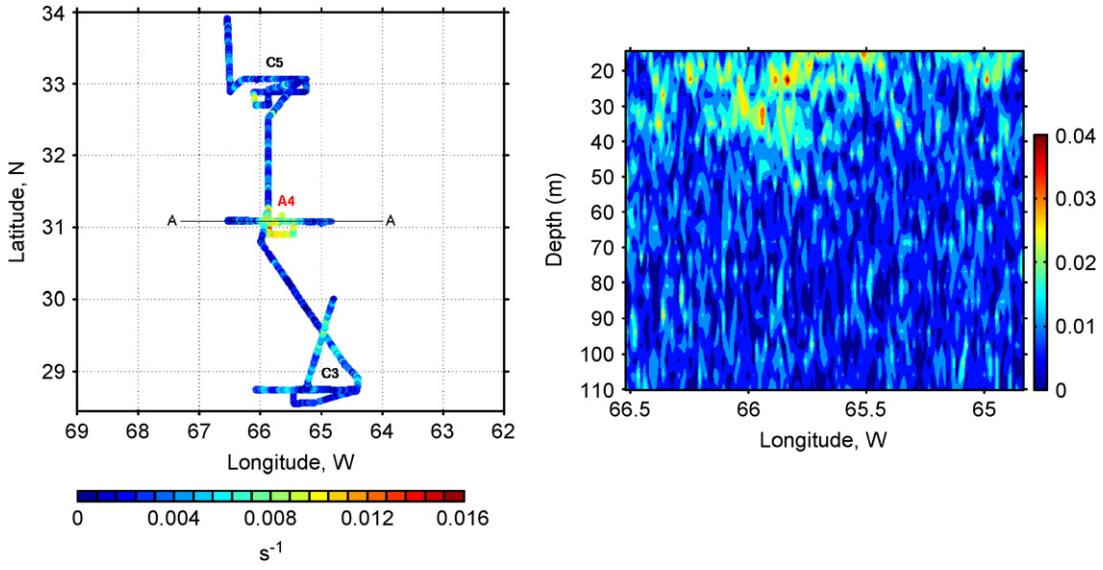

Fig. 24. Vertical shear averaged over the upper 50 m, computed from along track ADCP measurements 24–27 June 2005. Left panel: plan view along ship track; eddy A4 is at the center. Right panel: vertical section of vertical shear along the line AA in the plan view.

estimated nutrient flux at the center of the eddy was sufficient to maintain the most intense deep chlorophyll patch ever observed in the Sargasso Sea (McGillicuddy et al., 2007). This nutrient flux was due mostly to the vertical velocity, though it was augmented somewhat by turbulent diffusion, possibly enhanced near eddy center by trapped inertial waves. Convergence of diffusive buoyancy flux, and, more importantly, absorption of sunlight by the chlorophyll layer, caused the rate of upward displacement of isopycnal surfaces to be four times smaller than the actual vertical velocity, demonstrating the importance of diabatic processes in the accurate determination of the flux. These same processes would be important in the ecology of anticyclonic eddies in general and in the estimation of nutrient fluxes and new production in these eddies.

The submesoscale variability seen in the magnitude of the fluorescence peak in the chlorophyll maximum layer (Fig. 4) could be caused by the action of internal waves and other submesoscale dynamics causing short-term variations in the depth of isopycnal surfaces. Also there may be a feedback mechanism which causes patchiness to persist: as light is absorbed in a patch, it becomes buoyant relative to its surroundings, causing a diapycnal flux on the scale of the patch which preferentially brings nutrients into the area of the patch. This speculation deserves further consideration beyond the scope of the present work.

An effect that could further enhance nutrient fluxes into the euphotic zone, and lead to inhomogeneity in the chlorophyll distribution, is modulation of the upwelling velocity by variations of the relative vorticity across the eddy (e.g., Stern, 1965; Thomas and Rhines, 2002). The average upwelling resulting from this effect is much smaller than that due to variations in the surface stress across the eddy. However, if phytoplankton are able to take advantage of relatively brief (order of a day) uplift events, then there may be a covariance between the vertical velocity and the nutrient concentration, i.e. an additional vertical eddy flux of nutrients. This possibility deserves further consideration, careful account being taken of the statistics of upwelling following the fluid and the biological response to high-frequency variations in available light levels.

6.3. Implications for annual new production

A total vertical nutrient flux of 0.60 mmol N/m^2/d is about 40% of the flux required, basin wide, to drive the new production estimated from the oxygen build up during summer in the euphotic zone of the Sargasso Sea (Jenkins and Goldman, 1985; Spitzer and Jenkins, 1989; Sarmiento et al., 1990), the depletion in the oxygen minimum layer below the euphotic zone (Jenkins and Goldman, 1985; Jenkins and Wallace, 1992), and the seasonal Helium-3 cycle (Jenkins, 1988, 1998). However, the total vertical flux we measured is for the center of an eddy and therefore may be much greater than the average summer flux for the whole gyre. Hence, the source of nutrients required to drive the new production rates estimated for the gyre as a whole remains unknown. We note, however, that much greater nutrient fluxes may have occurred during the early development of this eddy, when biological processes responsible for the chlorophyll patch originally occurred (McGillicuddy et al., 2007).

7. Summary

A summary of the major results of this work is as follows:

(1) The deep chlorophyll patch in the center of Eddy A4, to our knowledge the most intense ever observed in the Sargasso Sea, was provided with DIN at a rate of at least 0.6 mmol/m^2/d by upwelling and diapycnal mixing.
(2) The nitrogen flux was not great enough, however, even if attributed to all mode-water eddies in the North Atlantic subtropical gyre, to provide enough nutrients to sustain annual new production believed to occur in the gyre.
(3) Theoretical estimates and a numerical model of the eddy show that the upwelling may have been driven by the wind-stress curl caused by the eddy surface current; the tracer results thus support the theory of Dewar and Flierl (1987) and Martin and Richards (2001).
(4) Solar heating was strong enough, even at the base of the euphotic zone, that the upwelling velocity was mostly diapycnal; isopycnal surfaces rose only one fourth as fast as the fluid itself.
(5) Diapycnal mixing at the base of the euphotic zone near eddy center was enhanced over background values for the ocean pycnocline. This enhancement was most likely a result of several intense storms passing over the eddy during the experiment, and diapycnal mixing may have been further augmented by trapping of near-inertial waves generated locally in the vorticity well of the anticyclonic eddy.

Acknowledgments

The officers and crew of the R/V *Oceanus* provided outstanding support during the seagoing operations. Essential technical support for tracer injection, sampling, and analysis was provided by Stewart Sutherland of LDEO, and by Brian Guest, Leah Houghton and Cynthia Sellers of WHOI, and by David Ciochetto. Blair Greenan, James Girton and Rebecca Walsh Dell assisted with tracer mapping during the cruises. Rick Boyce, Sherrie Witaker, James Dornicik, Louisa Bradtmiller, Penelope Howe, Nathan Buck and Rob Rember assisted with tracer sampling. Nutrient samples were processed by the Nutrient Analytical Facility (Paul Henderson) at WHOI. We gratefully acknowledge the efforts of all participants in the EDDIES project, which included a number of BATS

technicians. Numerical simulations were performed at NCAR's Scientific Computing Division. Valery Kosnyrev and Olga Kosnyreva assisted with data analysis and visualization, and Linda Cannata and Sue Stasiowski lent administrative support. The thoughtful and constructive comments of three reviewers are greatly appreciated. The EDDIES project was funded by the National Science Foundation Chemical, Biological, and Physical Oceanography Programs, Grant OCE 0241310. Additional support for remote sensing, including altimetry and QuikSCAT wind analyses, was provided by NASA.

Appendix A

The quasigeostrophic approximation for axisymmetric flow on an f-plane, with Ekman pumping dominating heating and diffusion in driving the system, reduces the potential vorticity equation to

$$\frac{1}{r}\frac{\partial}{\partial r}\left\{r\frac{\partial}{\partial r}\frac{\partial p}{\partial t}\right\} \approx f^2\frac{\partial}{\partial z}\left\{\frac{-1}{N^2}\frac{\partial}{\partial z}\frac{\partial p}{\partial t}\right\} \tag{A.1}$$

where r is the distance from center, z is the depth, t is time, and p is the perturbation pressure, f is the Coriolis frequency, and N is the buoyancy frequency (see Pedlosky, 1986, pp. 362–368). The horizontal length scale L of the problem is set by that of the boundary condition at the base of the Ekman layer $z = z_E$, which is

$$\frac{-1}{\rho N^2}\frac{\partial}{\partial z}\frac{\partial p}{\partial t} = w_E(r) \quad \text{at } z = z_E \tag{A.2}$$

If N^2 is not varying too rapidly and if the bottom is far away, then the vertical length scale arising in the problem is fL/N. For example if N were constant with depth and if $w_E(r)$ varied with r like Bessel's function of the first kind $J_0(r/L)$, then the solution for w would be $w = w_E(r)\exp\{-N(z_E - z)/fL\}$. For eddy A4 an appropriate value for L is 70 km, the density jump across the seasonal pycnocline gives a representative value of N of approximately $0.02\,s^{-1}$, and f is $7\times10^{-5}\,s^{-1}$, so the depth scale of penetration of the upwelling into the pycnocline would be $fL/N = 250$ m. This is far greater than the 60-m thickness of the pycnocline (Fig. 3), so one would expect the uplift driven by the asymmetry in the surface stress to be felt deep into the weakly stratified layer below. There are numerous coarse approximations made here, and we regard the numerical model described in Section 5 as more definitive.

References

Bibby, T.S., Gorbunov, M.Y., Wyman, K.W., Falkowski, P.G., 2008. Photosynthetic community responses to upwelling mesoscale eddies in the subtropical north Atlantic and Pacific Oceans. Deep-Sea Research II, this issue [doi:10.1016/j.dsr2.2008.01.014].

Bird, R.E., Riordan, C., 1986. Simple solar spectral model for direct and diffuse irradiance on horizontal and tilted planes at the earth's surface for cloudless atmospheres. Journal of Climate and Applied Meteorology 25, 87–97.

Buesseler, K.O., Lamborg, C., Cai, P., Escoube, R., Johnson, R., Pike, S., Masque, P., Mcgillicuddy, D.J., Verdeny, E., 2008. Particle fluxes associated with mesoscale eddies in the Sargasso Sea. Deep-Sea Research II, this issue [doi:10.1016/j.dsr2.2008.02.007].

Dewar, W.K., Flierl, G.R., 1987. Some effects of wind on rings. Journal of Physical Oceanography 17, 1653–1667.

Doney, S.C., 1996. A synoptic atmospheric surface forcing data set and physical upper ocean model for the US JGOFS Bermuda Atlantic Time-Series Study site. Journal of Geophysical Research 101, 25615–25634.

Falkowski, P.G., Ziemann, D., Kolber, Z., Bienfang, P.K., 1991. Role of eddy pumping in enhancing primary production in the ocean. Nature 352, 55–58.

Greenan, B.J.W., 2008. Shear and Richardson number in a mode-water eddy. Deep-Sea Research II, this issue [doi:10.1016/j.dsr2.2008.01.010].

Gregg, M.C., 1989. Scaling turbulent dissipation in the thermocline. Journal of Geophysical Research 94, 9689–9698.

Hayward, T.L., 1987. The nutrient distribution and primary production in the Central North Pacific. Deep-Sea Research 34 (9), 1593–1627.

Jenkins, W.J., 1988. The use of anthropogenic tritium and helium-3 to study subtropical gyre ventilation and circulation. Philosophical Transactions of the Royal Society of London A 325, 43–61.

Jenkins, W.J., 1998. Studying thermocline ventilation and circulation using tritium and helium-3. Journal of Geophysical Research 103 (8), 15817–15831.

Jenkins, W.J., Goldman, J., 1985. Seasonal oxygen cycling and primary production in the Sargasso Sea. Journal of Marine Research 43, 465–491.

Jenkins, W. J., Wallace, D., 1992. Tracer based inferences of new primary production in the sea. In: Primary Productivity and Biogeochemical Cycles in the Sea, pp. 299–316.

Knap, A.H., Michaels, A.F., Dow, R.L., Johnson, R.J., Gunderson, K., Sorenson, J.C., Close, A., Howse, F., Hammer, M., Bates, N., Doyle, A., Waterhouse, T., 1993. BATS Methods Manual. US JGOFS Planning Office, Woods Hole, MA.

Kunze, E., 1985. Near-inertial wave propagation in geostrophic shear. Journal of Physical Oceanography 15, 544–565.

Large, W.G., McWilliams, J.C., Doney, S.C., 1994. An oceanic vertical mixing scheme with a k-profile boundary layer parameterization. Reviews of Geophysics 32, 363–403.

Law, C.S., Watson, A.J., Liddicoat, M.I., 1994. Automated vacuum analysis of sulphur hexafluoride in seawater: derivation of the atmospheric trend (1970–1993) and potential as a transient tracer. Marine Chemistry 48, 57–60.

Leben, R.R., Born, G.H., Engebreth, B.R., 2002. Operational altimeter data processing for mesoscale monitoring. Marine Geodesy 25, 3–18.

Ledwell, J.R., Bratkovich, A., 1995. A tracer study of mixing in the Santa Cruz Basin. Journal of Geophysical Research 100, 20681–20704.

Ledwell, J.R., Watson, A.J., Law, C.S., 1998. Mixing of a tracer in the pycnocline. Journal of Geophysical Research 103, 21499–21529.

Levy, M., 2003. Mesoscale variability of phytoplankton and of new production: impact of the large-scale nutrient distribution. Journal of Geophysical Research 108 (C11), 3358.

Lewis, M.R., Cullen, J.J., Platt, T., 1983. Phytoplankton and thermal structure in the upper ocean: consequences of nonuniformity in chlorophyll profile. Journal of the Geophysical Research 88 (C4), 2565–2570.

Lewis, M.R., Harrison, W.G., Oakey, N.S., Hebert, D., Platt, T., 1986. Vertical nitrate flux in the Oligotrophic Ocean. Science 234, 870–873.

Martin, A.P., Richards, K.J., 2001. Mechanisms for vertical nutrient transport within a North Atlantic mesoscale eddy. Deep-Sea Research II 48, 757–773.

Martin, A.P., Richards, K.J., Law, C.S., Liddicoat, M., 2001. Horizontal dispersion within an anticyclonic mesoscale eddy. Deep-Sea Research II 48, 739–755.

McGillicuddy, D.J., Robinson, A.R., Siegel, D.A., Jannasch, H.W., Johnson, R., Dickey, T.D., McNeil, J., Michaels, A.F., Knap, A.H.,

1998. Influence of mesoscale eddies on new production in the Sargasso Sea. Nature 394, 263–265.

McGillicuddy, D.J., Johnson, R., Siegel, D.A., Michaels, A.F., Bates, N.R., Knap, A.H., 1999. Mesoscale variations of biogeochemical properties in the Sargasso Sea. Journal of Geophysical Research 104, 13381–13394.

McGillicuddy, D.J., Anderson, L.A., Doney, S.C., Maltrud, M.E., 2003. Eddy-driven sources and sinks of nutrients in the upper ocean: results from a 0.1° resolution model of the North Atlantic. Global Biogeochemical Cycles 17 (2), 1035.

McGillicuddy, D.J., Anderson, L.A., Bates, N.R., Bibby, T., Buesseler, K.O., Carlson, C., Davis, C.S., Ewart, C., Falkowski, P.G., Goldthwait, S.A., Hansell, D.A., Jenkins, W.J., Johnson, R., Kosnyrev, V.K., Ledwell, J.R., Li, Q.P., Siegel, D.A., Steinberg, D.K., 2007. Eddy-wind interactions stimulate extraordinary mid-ocean plankton blooms. Science 316, 1021–1026.

McNeil, J.D., Jannasch, H.W., Dickey, T.D., McGillicuddy, D.J., Brzezinski, M., Sakamoto, C.M., 1999. New chemical, bio-optical and physical observations of upper ocean response to the passage of a mesoscale eddy off Bermuda. Journal of Geophysical Research 104, 15537–15548.

Morel, A., Maritorena, S., 2001. Bio-optical properties of oceanic waters: a reappraisal. Journal of Geophysical Research 106, 7163–7180.

Niiler, P.P., 1969. On the Ekman divergence in an oceanic jet. Journal of Geophysical Research 74, 7048–7052.

Oschlies, A., 2002. Can eddies make ocean deserts bloom? Global Biogeochemical Cycles 16, 1106.

Oschlies, A., Garcon, V.C., 1998. Eddy-induced enhancement of primary production in a model of the North Atlantic Ocean. Nature 394, 266–269.

Oschlies, A., Garcon, V.C., 1999. An eddy-permitting coupled physical-biological model of the North Atlantic 1. Sensitivity to advection numerics and mixed layer physics. Global Biogeochemical Cycles 13, 135–160.

Payne, R.E., 1972. Albedo of the sea surface. Journal of the Atmospheric Sciences 29, 959–970.

Pedlosky, J., 1986. Geophysical Fluid Dynamics. Springer, New York.

Polzin, K., Toole, J., Schmitt, R., 1995. Finescale parameterizations of turbulent dissipation. Journal of Physical Oceanography 25, 306–328.

Sarmiento, J., Thiele, G., Key, R., Moore, W., 1990. Oxygen and nitrate new production and remineralization in the North Atlantic subtropical gyre. Journal of Geophysical Research 95, 18303–18315.

Schulenberger, E., Reid, J.L., 1981. The Pacific shallow oxygen maximum, deep chlorophyll maximum, and primary productivity, reconsidered. Deep-Sea Research 28A, 901–919.

Smith, R.D., Dukowicz, J.K., Malone, R.C., 1992. Parallel ocean circulation modeling. Physica D 60, 38–61.

Smith, R.D., Maltrud, M.E., Bryan, F.O., Hecht, M.W., 2000. Numerical simulation of the North Atlantic Ocean at 1/10 degree. Journal of Physical Oceanography 30, 1532–1561.

Spitzer, W., Jenkins, W., 1989. Rates of vertical mixing, gas exchange and new production: estimates from seasonal gas cycles in the upper ocean near Bermuda. Journal of Marine Research 47, 169–196.

Stern, M.E., 1965. Interaction of a uniform wind stress with a geostrophic vortex. Deep-Sea Research 12, 355–367.

Sweeney, E.N., McGillicuddy, D.J., Buesseler, K.O., 2003. Biogeochemical impacts due to mesoscale eddy activity in the Sargasso Sea as measured at the Bermuda Atlantic Time Series (BATS) site. Deep-Sea Research II 50, 3017–3039.

Thomas, L.N., Rhines, P.B., 2002. Nonlinear stratified spin-up. Journal of Fluid Mech. 473, 211–244.

Wanninkhof, R., Ledwell, J.R., Watson, J., 1991. Analysis of sulfur hexafluoride in seawater. Journal of Geophysical Research 96, 8733–8740.

Watson, A.J., Liddicoat, M.I., Ledwell, J.R., 1987. Perfluorodecalin and sulphur hexafluoride as purposeful marine tracers: some deployment and analysis techniques. Deep-Sea Research 34, 19–31.

Williams, R.G., Follows, M.J., 2003. Physical transport of nutrients and the maintenance of biological production. In: Fasham, M. (Ed.), Ocean Biogeochemistry: The Role of the Ocean Carbon Cycle in Global Change. Springer, Berlin, pp. 19–51.